NASA Public Access
Author manuscript
Geomorphology (Amst). Author manuscript; available in PMC 2021 November 15.

Published in final edited form as:
Geomorphology (Amst). 2021 November 15; 393: 107925. doi:10.1016/j.geomorph.2021.107925.

Inverted channel variations identified on a distal portion of a bajada in the central Atacama Desert, Chile

Rebecca M.E. Williams[a,*], **Rossman P. Irwin III**[b], **Eldar Z. Noe Dobrea**[a], **Alan D. Howard**[a], **William E. Dietrich**[c], **J.C. Cawley**[b]

[a]Planetary Science Institute, 1700 E. Fort Lowell, Suite 106, Tucson, AZ 85719, United States of America

[b]Center for Earth and Planetary Studies, National Air and Space Museum, Smithsonian Institution, PO Box 37012, MRC 315, Washington, DC 20013-7012, United States of America

[c]Earth & Planetary Science, University of California—Berkeley, 307 McCone Hall, Berkeley, CA 94720, United States of America

Abstract

In deserts, the interplay between occasional fluvial events and persistent aeolian erosion can form composite modern and relict surfaces, especially on the distal portion of alluvial fans. There, relief inversion of alluvial deposits by differential erosion can form longitudinal ridges. We identified two distinct ridge types formed by relief inversion on converging alluvial fans in the hyperarid Chilean Atacama Desert. Although they are co-located and similar in scale, the ridge types have different ages and formation histories that apparently correspond to minor paleoclimate variations. Gravel-armored ridges are remnants of deflated alluvial deposits with a bimodal sediment distribution (gravel and sand) dated to a minor pluvial phase at the end of the Late Pleistocene (~12 kyr). In contrast, younger (~9 kyr) sulfate-capped ridges formed during a minor arid phase with evaporite deposition in a pre-existing channel that armored the underlying deposits. Collectively, inverted channels at Salar de Llamara resulted from multiple episodes of surface overland flow and standing water spanning several thousand years. Based on ridge relief and age, the minimum long-term deflation rate is 0.1–0.2 m/kyr, driven primarily by wind erosion. This case study is an example of the equifinality concept whereby different processes lead to similar landforms. The complex history of the two ridge types can only be generally constrained in remotely sensed data. In situ observations are required to discern the specifics of the aqueous history, including the flow type, magnitude, sequence, and paleoenvironment. These findings have relevance for interpreting similar landforms on Mars.

This is an open access article under the CC BY-NC-ND license (http://creativecommons.org/licenses/by-nc-nd/4.0/).

*Corresponding author. williams@psi.edu (R.M.E. Williams).

Declaration of competing interest

The authors declare that they have no known competing financial interests or personal relationships that could have appeared to influence the work reported in this paper.

Appendix A. Supplementary data

Supplementary data to this article can be found online at https://doi.org/10.1016/j.geomorph.2021.107925.

NASA Author Manuscript
NASA Author Manuscript
NASA Author Manuscript

NASA Author Manuscript NASA Author Manuscript NASA Author Manuscript

Keywords

Fluvial landforms; Radiometric dating; Planetary geomorphology; Quaternary sequences

1. Introduction

Fluvial landforms preserved in inverted relief have been identified on all continents except Antarctica, and commonly are the remnants of continental river systems (e.g., Niem, 1974; Friend et al., 1979; Pain and Ollier, 1995; Williams et al., 2011, 2013; Foix et al., 2012; Miller et al., 2018). Despite the multitude of examples in depositional basins, few investigations have focused on alluvial fan settings subjected to relief inversion (e.g., Maizels, 1990). To fill this knowledge gap, we examined inverted channels located on a distal bajada in the Chilean Atacama Desert (Fig. 1).

Alluvial fans are cone-shaped landforms constructed where a river exits an upland and the sediment transport capability decreases (Harvey, 2011). Along a mountain front where multiple rivers debouche, alluvial fans coalesce into a bajada. In the hyperarid Atacama Desert, alluvial fans are an important record of regional hydrologic and climatic change (Hartley et al., 2005; Nester et al., 2007; Evenstar et al., 2009; Haug et al., 2010; Amundson et al., 2012; Ritter et al., 2018b) and this region includes some of the largest alluvial fans on Earth (e.g., the Arcas fan; Kiefer et al., 1997). Within the Pampa del Tamarugal (PdT, Plateau of the Tamarugal) basin, the bulk of basin infilling by alluvial and evaporite deposits occurred during the Late Miocene to Pliocene (Saez et al., 1999; Dunai et al., 2005). Reconstructing the depositional and erosional processes that modified these alluvial deposits to understand their relative timing, magnitude and rates is currently an active area of research (e.g., Jordan et al., 2014; Evenstar et al., 2020).

During the Quaternary, alluvial fan development in the central Atacama Desert have dominantly been influenced by 1) infrequent, high-magnitude fluvial flows (Houston, 2002; Pfeiffer et al., 2021), 2) strong diurnal surface winds (Hoffmeister, 2017; Muñoz et al., 2018), and 3) fluctuations in the water table that dissolve and precipitate solutes (Rech et al., 2002; Scheihing, 2018; Williams et al., 2017). A range of flow processes from fine-grained mudflows to high-energy floods transporting coarse sediment incise and onlap Pre-Pliocene deposits in response to intense, low-frequency (~decadal) precipitation events in the Precordillera Andes (Houston, 2002; Hartley et al., 2005; Pfeiffer et al., 2021). This complex, shifting interaction of various processes results in relict alluvial fan surfaces (Quezada et al., 2012), including former flow paths which are preserved in inverted relief (Jordan et al., 2014; Morgan et al., 2014).

In this study, we identify two adjacent varieties of inverted channels present on alluvial fans terminating in the Salar de Llamara. To our knowledge, this site is the first documentation of two disparate induration mechanisms—sulfate-capped and gravel-capped—for inverted landforms in close proximity. We characterize the morphology, sedimentology and mineralogy of these two types of inverted channels. We propose a developmental sequence for each ridge type, report new age constraints on depositional events, estimate the deflation

NASA Author Manuscript

NASA Author Manuscript

NASA Author Manuscript

rate, and draw connections between the geologic history and paleoclimatic conditions. Finally, we discuss general implications for the study of similar landforms on Mars.

2. Regional setting

2.1. Geologic setting

The relief setting for the PdT alluvial fans derives from the regional tectonics. In northern Chile, the Pampa del Tamarugal basin (also referred to as the Central Depression, 12,500 km^2) is a forearc basin resulting from subduction of the Nazca plate beneath the South American plate (Charrier et al., 2007; Nester and Jordan, 2011). This classic convergent plate margin produced several morphotectonic provinces across the study region; from west to east they are the Coastal Cordillera, the PdT basin, the Altiplano, the Precordillera, and the Andes (Fig. 1A and Supplementary Fig. S1). The Central Depression is a high-elevation plateau (~1 km above sea level [asl]) between N-S mountain ranges. To the west, the basin is bounded by the low-elevation (<2 km) Chilean Costal Range, an eroded Jurassic magmatic arc. Rising to the east of the PdT basin are the Andean foothills, called the Precordillera, and ultimately the towering (>3.5 km) Andes Mountains (Figs. 1A and S1). The volcanic arc has shifted eastwards since the Jurassic when it was beneath the Coastal Cordillera, to its current location under the Andes in the mid-late Miocene (Hoke et al., 2007; Charrier et al., 2007). North-trending, marginal faults of the Central Depression, called the Atacama Fault System to the west and the Precordillera Fault System to the east, formed due to extensional deformation (Saez et al., 1999; González et al., 2006). An extensive succession of non-marine sediments (Eocene to Pliocene) fills the PdT basin (Saez et al., 1999). The bulk of the PdT basin infill is sedimentary deposits, dominantly alluvial and fluvial deposits sourced from the eastern highlands, but lacustrine and playa deposits as well as interbedded volcanic layers are also present (Hartley and Evenstar, 2010). The basin fill varies in thickness due to subsurface paleorelief associated with folded Cenozoic basement rocks (Nester et al., 2007). East of Salar de Llamara, the basin fill is estimated to reach ~0.75 km thick, but elsewhere in the basin it reaches ~1.7 km (Labbé et al., 2019).

The Cenozoic stratigraphic sequence of the north Chilean forearc is described in detail by Hartley and Evenstar (2010), and we highlight units proximal to the study region for stratigraphic context (Quezada et al., 2012; Figs. 1B and S2). Much of the PdT sedimentary fill is strata within the Altos de Pica and El Diablo Formations (Galli and Dingman, 1962). These units are mostly conglomerates interbedded with poorly sorted sandstones that are dated between 20 and 12 Ma (Jordan et al., 2014). Pediment deposits uncomfortably overlie the El Diablo Formation, and are poorly consolidated gravels tens of meters thick. Lacustrine deposits are concentrated at the lower elevations within the PdT basin, and reflect changing water chemistry from freshwater to salt-pan conditions. These deposits include the anhydrite-rich Hilaricos Formation (upper Miocene), and the gypsum and halite evaporites of the Soledad Formation (early Pliocene).

The spatiotemporal extent of alluvial processes in the Atacama Desert provides ample record to compare with the ridges in this study. The PdT basin has been a major alluvial depocenter since the Miocene (Saez et al., 1999; Labbé et al., 2019), coincident with the uplift of the Altiplano ~26 Myra (Farías et al., 2005; Charrier et al., 2007). Surficial alluvial

NASA Author Manuscript NASA Author Manuscript NASA Author Manuscript

deposits span 30 to 100 km westward into the basin, and the uppermost ~10 m are relict deposits (poorly consolidated) from the Neogene (Jordan et al., 2014; Evenstar et al., 2017). These relict alluvial surfaces are part of a widespread pediment that extends over 1000 km N-S along the western flank of the Precordillera and collectively are called the Atacama Planation Surface (Evenstar et al., 2009), Pacific Paleosurface (Evenstar et al., 2017), or simply ‘pediment deposits’ (Quezada et al., 2012). Deep canyons called quebradas incise the Pacific Paleosurface, with some down-cutting up to >1.7 km, and local canyons have incised up to ~200 m (Jordan et al., 2014). At one site near the study region, incision of the pediment is estimated to have occurred ~7 Ma (21° 40′, the catchment of the Arcas fan; Kiefer et al., 1997).

Studies have delineated several alluvial surfaces that comprise the relict Pacific Paleosurface, (Jordan et al., 2014; Evenstar et al., 2017). Tectonic uplift and climate variations have resulted in cycles of alluvial aggradation, erosion and surface abandonment (Hoke et al., 2007; Nester and Jordan, 2011). Consequently, the PdT alluvial surface is a composite of relict and recent portions with the majority fossilized deposits from the Neogene. In the PdT, Jordan et al. (2014) identified at least four abandoned alluvial fan surfaces that date from 12 to 2.5 Myr and are correlated with short-lived climate cycles of hyperarid to arid conditions. The PdT alluvial fans enlarge and aggrade during wetter periods, followed by phases of depositional hiatus during hyperarid climates creating a multi-generational landscape. Relict fan surfaces are sequentially inset at lower elevation over time in response to base-level changes, with younger deposits of the bajada located towards the basin center. The geologic map of the study region and vicinity distinguishes relict alluvial deposits (pediment deposits, MPg) from Quaternary alluvial deposits, with the latter subdivided into ancient (PlHa) and active (Ha) (Fig. 1B; Quezada et al., 2012). This study examined the younger (Quaternary) portions of the bajada near the Salar de Llamara in areas mapped as active alluvial deposits by Quezada et al. (2012; Fig. 1B).

Quaternary alluvial fans in the Central Depression of the Atacama Desert record a wide variety of flow events, from floods to sheet-like mudflows (Houston, 2002). In the Tarapaca Province of Chile, mudflows were observed to have modest speeds (~4 m/s; e.g., Dingman and Galli, 1965). Mudflows range from exclusively fine-grain varieties, to clast-poor debris flows which have medium gravel clasts, to mudflows capable of delivering boulders and leaving lateral tracklines of boulders recording their paths (Kiefer et al., 1997; Morgan et al., 2014; Howard et al., 2016). Rheological changes can occur within the same flow event resulting in disparate deposit sedimentology and morphologies. Mather and Hartley (2005) document different flow rheologies that occurred in a single flow event in 2001; transitions between hyperconcentrated streamflow and mudflow occurred in response to different areas of the catchment receiving precipitation as the weather system moved across the Andean Precordillera. They propose a minimum three-stage progression in the 2001 event, with an initial phase of streamflow channel cutting, followed by mudflow that locally overtopped banks, and finally streamflow channel flushing. This spectrum of flow processes on PdT alluvial fans is collectively considered as ‘fluvial processes’ in this work because all involve running water to transport and deposit sediment within and adjacent to a water-carved channel.

NASA Author Manuscript NASA Author Manuscript NASA Author Manuscript

Together, these episodic, multi-phase flows and channel avulsions generate a complex network of active and abandoned channel segments on the alluvial fan surface. Wind deflation then etches differentially based on resistance to erosion and results in relief inversion. Weather stations document strong winds (~10 m/s to the northeast) that occur in afternoon hours on most days (Muñoz et al., 2018), and occasional wind speeds exceeding 25 m/s have been reported (e.g., Stoertz and Ericksen, 1974). Yardangs at the field site point to the northeast, consistent with the dominant wind direction. We consider this broad range of processes, both depositional and erosional, in evaluating the history of the PdT ridges.

2.2. Climatic and hydrologic setting

The regional climatic setting is a major control on where, when and how water reaches the PdT basin and modifies the desert landscape. The Atacama Desert is one of the driest deserts in the world, with average precipitation totaling <20 mm/yr (e.g., Clarke, 2006; Rech et al., 2006). For at least 13 Myr, the Atacama Desert has experienced mostly hyperarid conditions, and lesser aridity may extend back to the late Triassic (Clarke, 2006). Multiple factors combined to enhance aridity within the PdT, including the rain shadow that developed by the Andean orogeny, and reduced ocean vapor penetrating to the inland due to a) the Pacific high pressure cell that causes a temperature inversion in the atmosphere combined with b) cold oceanic currents, the Humboldt Current, that chills surface waters in the Pacific Ocean, and c) the topographic barrier of the Coastal Cordillera (Saez et al., 1999; Houston and Hartley, 2003). Surface denudation rates have been extremely low (~10 m/Myr) for the last ~15 Myr (Alpers and Brimhall, 1988). Many landscape elements have been preserved in this environment of overall long-term aridity and low surface denudation rates. Although most surface sediments were emplaced by 14.6 Myr (Evenstar et al., 2009), within the last 10 Myr, there have been local pluvial episodes that led to late Miocene to early Pleistocene incision and then stripping of the soil mantle (e.g., Amundson et al., 2012). Minor erosion or deposition on alluvial surfaces continued, including during the current period (e.g., Mortimer et al., 1974; Farías et al., 2005; Quang et al., 2005; Dunai et al., 2005; Nishiizumi et al., 2005; González et al., 2006).

Rainfall is rare within the PdT basin, but the highland paleoclimate impacted the water availability in the Central Depression, creating minor pluvial and minor arid events (Fig. 2; Santoro et al., 2017 and references therein). During the glacial-interglacial transition, multiple studies have documented at least two extended periods of increased rainfall in the Altiplano, called the Central Andean (or Atacama) Pluvial Event (CAPE I & II; Gayo et al., 2015; Ritter et al., 2019). Large high elevation paleolakes were present in the Altiplano during CAPE phases (e.g., Nester et al., 2007; Santoro et al., 2017). More water reached the PdT during CAPE phases and a few, shorter periods during the Late Holocene (including the Medieval Climate Anomaly), resulting in minor pluvial periods with more frequent overland flows (Fig. 2). During these somewhat wetter periods, precipitation in the Central Depression was still within the arid realm, with rainfall of ~100 mm/yr relative to the modern ~10 mm/yr (Amundson et al., 2012; Latorre et al., 2003). [In the hyperarid core, rain events >1 mm may only occur every 5–20 years (Ericksen, 1981).] Intervening dry periods in the PdT were characterized by rare surface flows, and small areas of groundwater upwelling. Such arid periods were regional-scale negative hydroclimate anomalies that

NASA Author Manuscript NASA Author Manuscript NASA Author Manuscript

occurred during a prolonged Mid-Holocene Dry Phase (centered on the Middle Holocene but extending beyond the temporal bounds of the subepoch) and intermittently during the Late Holocene (Nester et al., 2007; Santoro et al., 2017; Ritter et al., 2019). In the last 0.5 kyr, the Atacama Desert has experienced several brief “wet” periods identified based on radiometrically dated animal and plant matter from the region (e.g., Betancourt et al., 2000; Nester et al., 2007; Gayo et al., 2012, 2015).

Varying ephemeral playa-lake to perennial, shallow lacustrine conditions have occurred within the local terminal basin, Salar de Llamara, since the Late Miocene (Saez et al., 1999; Gayo et al., 2015). The lacustrine system once had a broad extent (minimum lake surface area of 2570 km^2; Ritter et al., 2018a) from the Llamara-Quillagua area eastward to the Salar Grande basin in the Upper Miocene-Pliocene, with thick evaporite sequences (up to 100 m) of the Soledad Formation as the remnants of this interconnected hydrologic system (Chong et al., 1999; Pueyo et al., 2001). In the Pleistocene, the Loa River breached the Coastal Range to reach the Pacific Ocean, an event that occurred no later than 274 kyr according to work by Ritter et al. (2018a). With this base-level lowering event, extensive water-carved dissection of the alluvial-lacustrine deposits occurred within the PdT basin (Saez et al., 1999; Chong et al., 1999; Pueyo et al., 2001). During the Quaternary, lakes and wetlands were occasionally present in the Atacama Desert (Pfeiffer et al., 2018). Within the Salar de Llamara basin, Quaternary playa deposits are delineated into two geologic units (‘ancient’ and ‘active’ playa deposits, $PlHa_p$ and Ha_p respectively) and record fluctuating lake levels (Fig. 1B; Supplementary Text S1, Figs. S1 and S2; Quezada et al., 2012).

With little direct precipitation in the Atacama Desert, both surface water and groundwater in the PdT are sourced from rainfall high in the Andes Mountains (e.g., Houston, 2002, 2009; Houston and Hart, 2004). Rivers have carved deep canyons into the mountain slopes and transported sediment westward into the PdT basin to form the bajada. Flows within the canyons are rare, with an approximately decadal recurrence interval in the modern era (e.g., Marker et al., 2012; Izquierdo et al., 2016; Wilcox et al., 2016). The groundwater table locally occurs near or at the surface, as evidenced by the presence of halophyte vegetation (especially *Prosopis tamarugo* trees concentrated along washes) and perennial brine pools (black arrow in Fig. 1A). Although the regional PdT groundwater system is complex and poorly understood, the perennial brine pool water chemistry combined with hydrologic modeling by Jayne et al. (2016) confirms aquifer recharge over different timescales from both shallow groundwater flow and deep, thermally driven groundwater emerging along basin fractures (Supplementary Fig. S1).

2.3. Study site setting

Our field site is located on the flanks of the Sierra de Moreno in the distal portion of converging alluvial fans between 20.5° and 21.5° S, centered at ~69.3° W. The site is on a bajada downslope from two canyons, with perennial flow through Quebrada Guatacondo and ephemeral flow in Quebrada de Pintados (Nester et al., 2007; Fig. 1A). Minor sediment contributions may have originated from Quebrada Mani. These canyons have incised the Pacific Paleosurface by 100–200 m.

NASA Author Manuscript NASA Author Manuscript NASA Author Manuscript

The catchment area covers ~1250 km^2 (incorporating the Guatacondo and Pintados canyons), and has a basin relief of ~3 km. Rocks in the catchment area include Jurassic-Paleogene conglomerates, sandstones, mudstones, and volcanic lithologies (andesite, dacite, rhyolite, and granodiorite) (Galli and Dingman, 1962; Ericksen, 1981), in addition to Miocene volcanic ash (Labbé et al., 2019) and early Miocene ignimbrite (van Zalinge et al., 2016).

Fan feeder valleys are 250–300 m wide at the apex, contain two or three active channels ~10–50 m wide, and incise older pre-Pleistocene alluvium. The fan slope decreases from 2° at the apex to 0.5° in the distal sections.

Along this bajada, the relative age of fan surfaces is easily distinguished in satellite images (Fig. 1C). The inactive portions of the fan are covered by dark wind-blown granules (few mm in size). The active zones on the bajada are <5 km wide and are typically pale yellow or very pale brown in color. Collectively the active tracts on the alluvial fan assemblage associated with the Guatcondo and Pintados canyons are within an area of <100 km^2.

Incised channels are present within the active zone, with dimensions of 3–12 m wide and ~1 m deep. Elevation surveys in the mid-fan section revealed relief variations of several meters, including channel overbank deposits 1 m above the fan surface, and inverted channels up to 2 m in relief (Morgan et al., 2014). Overbank mudflow deposits can extend bilaterally up to 150 m from the channel (Morgan et al., 2014).

The pronounced temporal difference (frequency, rate and duration) between alluvial accumulation versus longer-term aeolian deflation has a discernible, cumulative effect on alluvial fans where old flow paths may be preserved as elevated landforms. The study region includes several ridge forms on the distal bajada previously interpreted as inverted channels (Morgan et al., 2014), and shown here to have varied attributes and formation history (Fig. 1C). The ridge forms are aerially extensive features that can readily be identified and mapped in satellite images, with a darker tone that contrasts with the lighter tone of mudflow deposits that blanket the lowlands. On the ground, they present as ridges that are 1–2 m in relief and extend >0.5 km in length. In places, the ridges include relict in situ woody plant fragments.

3. Methods

The observation that distal bajada ridges in the PdT differ motivated this study to characterize their physical attributes and investigate ridge origin. Landform shape and appearance are described at a range of scales, from both the aerial and ground perspective. To constrain ridge formation processes and sequence, we consider the geologic context, field relationships, ridge composition (grain size and mineralogy) and age.

Satellite data for the field site included Quickbird images acquired on November 20 and December 3, 2008, both with a resolution of 0.60 m/pixel, and satellite images (Google Earth, 2013). Information on satellite images used in this study is provided in Supplementary Table S1.

NASA Author Manuscript NASA Author Manuscript NASA Author Manuscript

Field studies, measurements, and observations at the ridges were conducted between the years 2010 and 2017. Topographic surveys used the Trimble Pro XRS Differential Global Positioning System (DGPS), with 2–4 cm horizontal and vertical precision in the acquired elevation data. Elevation measurements are used to characterize ridge shape with spot points acquired along longitudinal and cross-sectional ridge transects.

Multiple, standard methods were employed to characterize grain size. We used the Wentworth scale for grain size classification with sand <2 mm, gravel 2–64 mm, and cobble >64 mm. In outcrops, we visually estimated the percent frequency by area of cobbles, gravels and sand (or finer) clasts. This observation was translated to a qualitative facies name by plotting the percent frequency on a grain size ternary diagram following the nomenclature of Buffington and Montgomery (1999; Table 1). Gridded clast counts (0.2 m^2 areas with a 5 cm grid) were also conducted both on the surface and in vertical section following methods in Bunte and Abt (2001). For mudflow deposits, sediment grain size distributions were based on laboratory laser diffraction analysis of dispersed samples.

Mineralogy was constrained in the field using a portable, battery-operated Olympus Terra X-Ray Diffraction (XRD) system (Blake et al., 2012). XRD analyses were performed using the commercially available software XPowder. Quantitative estimates of relative abundances (weight percent) derived from the XRD pattern were performed using Reference Intensity Ratios methods. Spectral measurements were acquired in the visible through near-infrared (VNIR – 350–2500 nm) wavelengths, converted to reflectance relative to Spectralon, and analyzed by using a combination of Tetracorder and visual comparison of the calibrated spectra with laboratory spectra available in the U.S. Geological Survey spectral library (Kokaly et al., 2017).

We sampled in situ fossil wood embedded in four ridges, and one mudflow deposit to determine chronology (Table 2). These woody plant fragments appeared to be in growth position, including root systems. Wood fragments were cut to obtain an interior component weighing 1 g and submitted for accelerator mass spectrometry and bulk radiocarbon dates. All samples were analyzed at the National Ocean Sciences Accelerator Mass Spectrometry (NOSAMS) facility. Radiocarbon ages were calibrated with CALIB 7.1 using the terrestrial calibration curve for the Southern Hemisphere (SHCal13, Hogg et al., 2013; Stuiver et al., 2019), intercept method and 2-sigma (2σ) confidence interval. All ages reported here are given in thousands of calendar years before 1950 (kyr) and rounded to the nearest 10 yr.

4. Results

We identified two distinct ridge types on the alluvial fans that terminate in the Salar de Llamara. Ridges are present on the distal bajada, first appearing ~30 km from the fan apex relative to the ~40 km total fan length. In the next two sections, we highlight observations from segments for each ridge type (gravel-capped ridge R1 and sulfate-capped ridge R4) within the study site (Fig. 1C).

NASA Author Manuscript NASA Author Manuscript NASA Author Manuscript

4.1. Gravel-capped ridge characteristics

Multiple gravel-capped ridges are present in the PdT (Morgan et al., 2014). Three gravel-capped ridges occur within the study region (R1, R2, and R3; Fig. 1C). This ridge type is characterized by a monolayer of coarse gravels (typically 1–3 cm long-axis) on the surface (Figs. 3A and 4A).

The longitudinal slope of the top of the gravel-capped ridge parallels the regional gradient (Fig. 5). Ranging up to 2.5 km in length, these curvilinear ridges sometimes bifurcate downslope (Fig. 6). Gravel-capped ridges are 1–2 m in relief and typically have a triangular transverse cross-sectional shape (Figs. 3A and 5D).

The gravel-capped ridges generally have weak to no induration of the sediment, especially in the upper ~0.5 m. Therefore, the upper component of this ridge type is readily disturbed when walked upon and easily excavated with bare hands to move the largely unconsolidated sediment (Fig. 7). Thin (<1 mm) efflorescent surficial salt crusts do occur (Fig. 7B). Salts producing well-indurated components of these ridges have a patchy occurrence as nodular evaporites (halite) and, where present, are located on the lower ridge flanks.

Beneath the gravel monolayer, very poorly lithified sediment within the ridge is dominantly fine-grained (Fig. 7). Within a shovel-dug trench, the upper 10 cm is a weakly laminated, sand-rich unit that sits atop a massive, poorly-sorted unit with occasional matrix-supported gravels (Fig. 7C and D).

A pronounced change in the surficial grain size distribution is observed from the crest downslope to the lowlands of gravel-capped ridges (Figs. 8 and 9). The coarsest clasts are on the ridge crest. A representative sample of the crest surface is shown in Fig. 9D, with fine gravel clasts common. In rare locations, small cobbles are observed (Fig. 8). Clast size decreases downslope across the ridge flanks to the lowlands (Fig. 8). Gravels and cobbles are subrounded to subangular in shape, and composition matches the diverse rock types in the catchment.

Using the facies classification scheme of Buffington and Montgomery (1999; Table 1), the gravel-capped ridge surface is a cobbley, sandy gravel facies, whereas the interior ridge sediment is a gravelly, sand facies (Figs. 9D and 7C–D, respectively). The difference in sediment size distribution between these facies is also evident in clast counts conducted at the ridge surface and within the excavated trench (Fig. 10). The dominant grain size within the ridge is sand, whereas the majority of clasts on the surface are fine gravel or larger.

4.2. Sulfate-capped ridge characteristics

Sulfate-capped ridges (e.g., R4 and R5 in Fig. 1C) constitute a newly recognized variety of inverted channel ridge form, characterized by their multi-layer salt cap that is several tens of centimeters thick (Figs. 3B, 11 and 12). Two sulfate-capped ridges occur within the study site, and we highlight observations made at ridge R4.

In aerial images, these ridges have a darker tone than the pale tan mudflows bordering the ridge, but they are not readily distinguishable from the nearby gravel-capped ridges (Fig.

NASA Author Manuscript NASA Author Manuscript NASA Author Manuscript

1C). Typical ridge length is 0.5 km. The planform for sulfate-capped ridges has branches that merge downslope, such as at ridge R5 (Fig. 6B). Ridge R4 has two short (<20 m) spurs with junction angles that point downslope along its linear length (Figs. 3C and 12A).

At outcrop scale, several differences are noted for the sulfate-capped ridges relative to the gravel-capped ridges in the study site. Sulfate-capped ridges have a rectangular to trapezoidal cross-sectional shape (Figs. 3B, D and 11A). The ridge top surface ranges from 0.5 to 3 m in width and is slightly concave with a raised margin (Figs. 3D and 12B).

Overall grain sizes are finer in the sulfate-capped ridge than in the gravel-capped case. Gravels are sparsely present on the ridge top and increase in frequency on the slope, with the highest concentration in the lowlands (Figs. 8 and 9). This is inverse to the pattern observed at gravel-capped ridges. One exception to this general relationship is at ridge R5, where local concentrations of cobbles (low-density ignimbrite) are observed on the ridge flank (Fig. 11D). Similar ignimbrite clasts are reported up-fan along flow margins by Morgan et al. (2014), and at other Atacama alluvial fan sites with boulders that have rafted a few kilometers from their source (Mather and Hartley, 2005).

Our study of ridge R4 included excavating a trench at the northeastern end and sample collection. The R4 ridge is well indurated, a qualitative assessment based on the difficulty in exposing the vertical section. Color, grain size, competency and bedding geometry are the primary criteria for identifying layers in the excavated outcrop. Layers at the base of the outcrop are planar-bedded, in contrast to the concave-upward layers at the top of the section (Fig. 13). The concave shape is particularly evident at the base of two resistant layers (Fig. 13B), as well as in a prominent, thin (5 cm) orange layer.

All R4 layers were fine-grained with no laminations present. Silt-sized sediment is present throughout the section, with variable amounts of fine to medium sand concentrated in five distinct layers (sand facies). A small gravel-rich lens (0.2 cm wide × 0.05 cm high; clasts 0.2–0.5 cm b-axis) is present in a fine-grained sandstone at the boundary of the lower and upper units. This gravelly sand facies is the only observation of sediment coarser than sand within the R4 outcrop (Fig. 13C). Rock types within the gravel lens match the lithologies observed at the gravel-capped ridges.

Detailed mineralogical and spectral information for R4 layers is reported and discussed in Noe Dobrea et al. (2017; ridge R4 is referred to as ‘WIN’ in that paper). Significant amounts of sulfates, predominately anhydrite, are present throughout the ridge R4 volume (XRD mineral abundance >50 wt%), but the upper section is largely devoid of primary minerals except for very minor amounts of quartz. Based on this compositional distinction, we subdivided ridge R4 into upper and lower units (Fig. 14; see Supplementary Text S2). The R4 lower unit is composed of primary minerals (muscovite, plagioclase, and quartz at cumulative abundances >30 wt%) and evaporites (dominantly anhydrite and halite). In contrast, an ~0.4 m thick upper unit is almost entirely (>85 wt%) evaporite minerals (sulfates and chlorides), with very minor quartz abundance (<3 wt%) and the residual <10 wt% is amorphous. The upper unit has substantial amounts of anhydrite (>70 wt%), except near the top where gypsum is also present.

NASA Author Manuscript NASA Author Manuscript NASA Author Manuscript

Salts dominate the mineralogy throughout the ridge volume. Anhydrite and halite are present in all layers. Several sulfate minerals are also observed in discrete layers, with gypsum, jarosite, and glauberite identified. Two hardpan layers in the lower unit were nearly impenetrable with a pickaxe, have relatively high anhydrite abundance (~75 wt%), and are locally correlated with a yardang remnant of ancient alluvial/playa outcrops (Supplmentary Fig. S3). The flanks of ridge R4 have a thin (~1 cm) slope-conforming salt layer composed of halite. Within the central portion of the outcrop (part of the lower unit), color is correlated with mineralogy: the thin orange layer, as well as the splotchy reddish-yellow and pinkish-white coloration in mottled layers (Fig. S4; Table S2 in supplmentary information) are attributed to jarosite.

Evidence of plants and possibly subsurface organisms is noted at ridge R4. Root holes, iron-stained root casts, and bioturbation texture are observed. Three wood fragments were found in the upper unit, but none were found below 0.5 m.

Ridges R4 and R5 are partially covered with loose, small (<15 cm), thin (~1 cm) sulfate plates that range from disk-shaped to hollow domes (up to several cm relief) (Figs. 9C and 12C–E). On the upper surface of the sulfate plates, a pervasive rough surface texture of closely spaced ~2 mm-across bumps (similar to goosebumps) is commonly observed (Fig. 12E). The sulfate plates have an irregular bulbous underside surface that is not completely in contact with the underlying substrate. Compositionally, the plate's top surface is gypsum, but the underside is dominated by anhydrite (Noe Dobrea et al., 2017).

4.3. Radiometric age results

Nine in situ wood samples from the study site were radiometrically dated and provide a record of conditions wet enough to foster woody vegetation. Wood samples were collected from three gravel-capped ridges (two samples from ridge R1, and one each from ridges R2 and R3), the sulfate-capped ridge R4 (three samples), a mesa near the downslope terminus of ridge R1, and a mudflow. Sample details including geographic location are provided in Table 2, and field photos of samples are in the supplementary information.

Our ^{14}C chronology has two distinct clusters of calibrated ages (~9.3 and ~11.9 kyr) that are associated with the two ridge types (Fig. 15). The oldest age cluster from samples collected at gravel capped ridges spans the Late Pleistocene to Early Holocene. Dates for wood samples collected from the surface of R1 at nearby sites (<10 m apart) yielded 2σ dates that did not overlap (11,930–12,320 yrs BP for R1-A and 11,400–11,850 yrs BP for R1-B). Other gravel-capped ridges (R2 and R3) in the area where wood was collected had similar calibrated ages between 11 and 12.5 kyr.

The second age group includes three wood samples from the sulfate-capped R4 ridge. Two specimens in growth position were obtained 30–50 cm below the R4 surface and yielded consistent ^{14}C calibrated ages (2σ between 9030 and 9500 ^{14}C yrs BP), whereas a sample from closer to the surface had a distinctly younger age (8160–8340 ^{14}C yrs BP). These decreasing ages up section are consistent with episodic wet intervals at R4. One specimen obtained from a mesa ~180 m SE from R1 had an age (9270–9500 ^{14}C yrs BP) that

NASA Author Manuscript

NASA Author Manuscript

NASA Author Manuscript

overlapped with the older R4 specimens (R4-B & R4-C). It suggests that this area (~800 m asl) may have been wet at this time (Fig. 15B).

Wood embedded in a mudflow deposit (MudX) near R4 had the youngest age (~1 kyr; Fig. 15B). This date provides a constraint for mapped ‘active alluvial deposits’, extending back at least into the late Holocene. (See Supplementary Text S3 for description of two mudstone facies mapped as ‘active alluvial deposits’; Howard et al., 2016).

5. Discussion

5.1. Differences in ridge formation

The two ridge types differ in their capping material, sedimentary characteristics, stratigraphic context, landform shape, and planimetric configuration. We interpret both ridge types to be inverted channels because they are fluvial sedimentary deposits that are more resistant to erosion than surrounding materials and therefore expressed in positive relief. However, based on their dissimilarities, the ridges clearly did not originate in the same manner.

One main distinction between the ridge types is compositional, with a succession of sulfates characterizing one type, and the relatively minor presence of such salts within and atop gravel-capped ridges on the other. This compositional difference is directly related to the competence of the upper ridge R4, with well-indurated sulfate-capped ridges in contrast to the unconsolidated deposits with minor to no cement at the gravel-capped ridges. Some gravel-capped ridges have well-indurated units at depth, such as the mudstone layers in Supplementary Fig. S11C–D, or the subsurface (~0.5 m) cemented core of halite nodules at another site ~5 km downfan (21.139629° S, 69.651342° W). We interpret these attributes as unrelated to or a minor influence on the formation of the ridge during relief inversion.

Grain size also differs for the ridge types, both at the surface and throughout their vertical sections. Gravel-capped ridges are pebbly sand deposits with the coarse fraction concentrated on the ridge exterior surface. Although there are a few gravels on the sulfate-capped R4 ridge surface, sediment coarser than medium sand is largely absent in the vertical section and observed only in a gravel lens (Fig. 13C).

The branching pattern for gravel-capped ridges, with junction angles pointing upslope, matches that of a distributary channel system on an alluvial fan (Fig. 6A). In contrast, the sulfate-capped ridges exhibit downslope merging, and could be relics of a tributary channel system (Fig. 6B). Potentially, ridge R4 may have been linked to ridge R5, a similar sulfate-capped ridge ~500 m to the southwest (Figs. 1C and 11). Furthermore, a few kilometers down gradient from the study site, a comparably scaled contributory channel network is incised into ancient playa deposits (Fig. 16). This example may be analogous to the setting for sulfate-capped ridges prior to relief inversion.

Although we found a down-gradient transition in ridge type at the study site (gravel-capped ridges are upslope from sulfate-capped ridges), this pattern is not universally observed in this area. There are gravel-capped ridges further downslope in the Salar de Llamara basin

NASA Author Manuscript NASA Author Manuscript NASA Author Manuscript

(e.g., at 21.139629° S, 69.651342° W). Therefore, the ridge type is not strictly bound by location (elevation) on the bajada. Interestingly, gravel-capped ridges cease at a maximum elevation consistent with the upslope extent of mapped ancient playa deposits (Fig. 1B dashed red line), which would be consistent with concurrent deposition in the playa and the stream channels that debouched into it.

5.1.1. Gravel-capped ridges—A key to understanding the formation of gravel-capped ridges is the interpreted relationship between the two unconsolidated sedimentary facies observed at ridge R1. We attribute the difference in grain size distribution between the surface and interior of gravel-capped ridges to removal of fine sediment by erosion, resulting in a coarser surface lag deposit (Fig. 10). The gravelly, sand facies that comprises the ridge volume is particularly susceptible to deflation-generated clast armoring (Fig. 17A–B). Removal of fine sediment by aeolian winnowing leaves a gravel lag that ultimately armors the underlying sediment and inhibits further deflation (e.g. McFadden et al., 1987). The formation of inverted channels in many arid environments is attributed to this clast-armoring mechanism (e.g., Maizels, 1990; Miller et al., 2018; Zaki et al., 2018, 2021).

If this interpretation is correct, then the interior of the ridge deposits should have a clast distribution that more closely matches the original flow deposit than the surficial armor. We consider a mudflow as the most likely flow type for the R1 deposit, although we cannot rule out streamflow processes. The poorly sorted R1 interior deposit with matrix-supported gravels is consistent with a mudflow deposit. In addition, modern mudflow deposits located upslope in Quebrada de Guatacondo (Morgan et al., 2014) have a similar grain size distribution to the gravelly, sand facies that constitutes the ridge R1 interior deposit (Table 1).

5.1.2. Sulfate-capped ridges—The layered sequence in ridge R4 records episodic development with wet periods, as evidenced by root fragments and iron-stained plant molds, and dry intervals that are marked by salt hardpans at some layer boundaries. An overly simplified scenario for the formation of the sulfate-capped ridge R4 can be summarized into four stages:

1) episodic deposition of sediments that constitute the lower unit, 2) channel incision into these deposits, 3) precipitation of an evaporitic sequence within the channel to form the upper unit, and finally 4) erosion to create the ridge. For additional details on the complex early history of R4 involving deposition, sub-aerial exposure and diagenetic alteration based on work by Noe Dobrea et al. (2017), see supplementary information Text S2. In this section, we focus the discussion on the later history of ridge R4 development.

The precursor stage in development of the R4 upper unit is the creation of a channel (Fig. 17-D1), reflected in the concave-up cross-sectional form of some layers. The channel substrate is presumably ancient alluvial/playa deposits (Fig. 1B and Supplementary Figs. S2 and S3). The original R4 channel likely formed by channelized flow that caused incision (streamflow case) or, alternatively, was the result of an aggradational channel with levees (mudflow case). Both types of modern channels are present at this site, and conceivably both flow types are recorded in the R4 section (Supplementary Text S2). Overbank deposits can

NASA Author Manuscript NASA Author Manuscript NASA Author Manuscript

include low density ignimbrite cobbles that concentrate along the flow margins, as observed at ridge R5 (Fig. 11D), and reported up-fan by Morgan et al. (2014) and at other Atacama alluvial fan sites where they have rafted a few kilometers from their source (Mather and Hartley, 2005).

Repeated flows within the channel formed draping sand layers (i.e., not bedforms, Fig. 17-D2). The fine to medium gravel lens at the lower-upper unit boundary (Fig. 13C) is evidence for a final streamflow event that deposited pockets of coarser sediment. The uppermost layer of the lower unit also has root casts and gypsum, suggesting development of a weak paleosol after streamflow ceased.

The R4 upper unit has mineralogical and morphological attributes that are consistent with a chemical deposit (Noe Dobrea et al., 2017). The prevalent salt composition (crystalline mineralogy is salt except for ≤3 wt% quartz), minute presence of primary minerals (presumably aeolian sediment), and concave-up form of the layers suggests that the upper unit is an evaporite sequence that precipitated within the R4 channel (Fig. 17-D3).

Pedogenic crusts (such as gypcrete) form when solar evaporation drives precipitation in a salt-saturated surface or near-surface brine (Watson, 1988; Aref, 2003; Warren, 2016). Subsurface crusts form during evaporation from the capillary fringe above the water table. Alternatively, salt precipitation can occur in ponded water. We favor direct salt precipitation in water to form the salt rich R4 capstone because of the lack of detrital sediment or sediment displacive textures.

Salt precipitation occurred in stages to form the layers of the R4 upper unit. Truncated plant roots in at least one layer indicates the periodicity of salt formation (Supplementary Text S2). Inflow into the inactive R4 channel was associated with a variable water table level that, at times, may have rose to ~800 m asl. The water table may have fluctuated in tandem with lake levels, or due to recharge associated with infiltration of local runoff, increased precipitation in the Altiplano, or some combination of these factors.

Although the R4 capstone is anhydrite-rich, it is likely that the original salt mineralogy was dominantly gypsum, which is the thermodynamically stable phase of calcium sulfate below 40 °C (Hardie, 1967). Dehydration processes transform gypsum to anhydrite. Extraction of crystalline-bound water within gypsum can occur in arid environments as well as in acidic aqueous environments (e.g., Zanbak and Arthur, 1986; Azimi and Papangelakis, 2011). Microorganisms can facilitate this mineralogy transformation, as has recently been documented in Atacama sulfate specimens by Huang et al. (2020). The co-existence of gypsum and anhydrite in the topmost section of ridge R4 may reflect incomplete dehydration. This mineralogical transformation can result in volume reduction of up to 40% (Azam, 2007), but no signs of significant shrinkage in ridge R4 (e.g., polygonal cracks, gulls, etc.) are evident. Gypsum precipitation was apparently rapid to form the microcrystalline deposit (mesoscale crystal forms are only present in the lower unit; Supplementary Fig. S4). Alternatively, Voigt et al. (2020) argued that the most likely scenario for the formation of anhydrite in the Central Depression of the Atacama Desert was direct precipitation in a fluid with high salinity.

NASA Author Manuscript NASA Author Manuscript NASA Author Manuscript

Evidence for groundwater emergence is pervasive in the region with dissolution features and perennial brine pools (Stoertz and Ericksen, 1974; Williams et al., 2017; Voigt et al., 2020). Within the Salar de Llamara pools located ~17 km SSW from the field site (Fig. 1A, Supplementary Figs. S5 and S6), Rasuk et al. (2014) documented modern gypsum precipitation; a similar groundwater-fed environment may have been present at R4 enabling the precipitation of gypsum with subsequent dehydration to anhydrite. Also, diagenetic alteration of layers in the lower unit as well as displacive growth of macrocrystalline gypsum (Supplementary Fig. S4) could be related to groundwater processes (Supplementary Text S2). The layered R4 capstone indicates multiple periods of standing water, so conceivably water sourced from groundwater or ponded surface flows both occurred, at least intermittently, over a >1 kyr period.

Finstad et al. (2016) estimated that the average salt formation rates for the Atacama Desert over geological time are relatively rapid (0.03 $mm \cdot m^{-2} \cdot d^{-1}$). Therefore, sulfates in the upper unit could have formed in a few decades based on the ~0.4 m thickness. Dated wood samples from ridge R4 were collected at several decimeters depth and provide constraints on the timescales for capstone development. Computed average vertical formation rates for the three R4 specimens range from 0.03 to 0.05 mm/yr, which is less than 1% of the rate reported by Finstad et al. (2016) and further supports the episodic emplacement of sulfate.

The loose sulfate plates capping ridge R4 may be unrelated to or a minor factor in the relief inversion process. Their origin is not well understood. The sulfate plates are not observed in the R4 stratigraphic section, and therefore they must have formed in a different microenvironment or were modified from their original form. Sulfate plates are observed elsewhere in the Salar de Llamara. They are present in isolated occurrences associated with both curvilinear ridges and mesas. Two examples of mesas capped with sulfate plates within the study region are illustrated in Supplementary Fig. S7. We speculate that the sulfate plates atop R4 are remnants of sulfate endoevaporitic forms based on similarities to modern examples (e.g., Rasuk et al., 2014) including comparable geomorphic attributes (dome to platform hollow forms) and configuration (patchy, quasi-circular distribution on surfaces). If valid, formation of the sulfate plates may reflect factors such as the water chemistry and longevity of ponded water that differed from earlier periods in the development of ridge R4 (Fig. 17-D4). Additional study is needed to investigate this hypothesis (Supplementary Text S4). An alternative explanation for the sulfate plates proposed by Noe Dobrea et al. (2017) invokes fog in repeated dissolution and re-precipitation of calcium sulfate (Rech et al., 2003), potentially on a daily cycle.

5.1.3. Deflation rate in ridge formation—Widespread aeolian erosion exposed the channel infilled R4 evaporites and generated ridges that are gravel capped. The dominant wind direction is generally parallel to the ridge axis, an alignment that may have aided in relief inversion. Evidence of aeolian erosion are in yardangs, the wind-sculpted ancient alluvial/playa remnants that are oriented southwest to northeast (Figs. 3B, 4A, 12 and S3). Regional deflation of up to 1.5 m occurred. The age-dating results at R4 suggest a minimum deflation rate of 0.2 m/kyr. A somewhat lower rate of ~0.1 m/kyr is computed for R1, R2 and R3, if erosion was initiated immediately after flow events. However, it is possible that the deflation rate was higher if the ridges were stabilized. Two factors that may further

NASA Author Manuscript

NASA Author Manuscript

NASA Author Manuscript

protect the ridges from additional erosion are salt deposits that have formed on the ridge flanks, as well as relatively young mudflows (<1 kyr) that surround the ridges filling in the lowlands. These estimated erosion rates are slightly lower than the long-term average erosion rate of ~0.3 m/kyr estimated for the Arcas fan, located ~65 km to the south (Kiefer et al., 1997).

5.2. Comparison to terrestrial inverted channels

This is the first documented site, to our knowledge, of co-located inverted channels with different induration mechanisms and formation scenarios. In a literature review of >100 inverted channel examples on Earth, Zaki et al. (2021) found that nearly a quarter are channels filled by volcanic materials, relatively few cases are gravel-capped ridges (<10%), and the majority are cemented fluvial deposits (includes surface and subsurface cementation). This study adds to the inventory of terrestrial inverted channels with two types that are co-located on a bajada: gravel-capped and sulfate-capped. Importantly, the sulphate-capped ridges studied at Salar de Llamara are composed of an evaporite capstone atop fluvial sediments, rather than cemented fluvial deposits. Thus, this example constitutes a new variation for inverted channel formation, one that involves infilling the channel with an evaporite sequence.

5.3. Relationship between inverted channel shape and former flow dimensions

To what degree does the scale of the Salar de Llamara inverted channels reflect the former flow? The answer differs based on ridge type due to their unique formation scenarios. We use field observations to estimate former channel dimensions and compare them with ridge scale. Modern channels present on this bajada (~1 m depth, 3–10 m width; Morgan et al., 2014) are a useful benchmark to compare with inverted channel dimensions.

For the sulfate-capped ridges, the original channel dimensions appear to be well reflected in the R4 capstone shape (e.g., maximum thickness of ~0.5 m and width of 3 m), consistent in scale with the narrower modern channels. The inferred formation mechanism for this ridge type, evaporites deposited within the channel, would preserve channel width in the ridge top width prior to any erosional retreat.

The minimum streamflow depth can be constrained based on gradient (0.005) and the coarser fraction of sediment size (e.g., adopting D_{84} = 0.8 cm based on the medium gravel in Fig. 13C). Following Dietrich et al. (2017; equation 28.8), the threshold depth over this gradient to mobilize medium gravel at ridge R4 is ~0.1 m, assuming particle density of 2.65 g/cm^3. However, this approach neglects channel wall stress. As the width to depth ratio falls below about 8 the proportion of the total boundary shear stress applied to the banks increases, leading to greater flow depths to initiate gravel transport. For reference, in the case of a rectangular channel with a width to depth ratio of 3 (the size and shape of small channels here), the proportion of the total stress applied to the banks is about 38% (e.g. Knight et al., 1984) and the predicted flow depth to initiate the medium gravel transport would then be ~0.15 m. Even with this correction, relatively shallow flow depths are sufficient to transport gravels. The paleo-depth estimates are less than modern channel depth, and significantly less than the corresponding ridge height. The discharge was likely

NASA Author Manuscript

NASA Author Manuscript

NASA Author Manuscript

modest (<1 m^3/s) based on these estimated flow dimensions and a computed average flow velocity of a few tenths m/s (e.g., equation 28.11 in Dietrich et al., 2017).

For the gravel-capped ridges, there is greater uncertainty in the original flow and deposit dimensions. There is no obvious sedimentary sub-division within the ridge to indicate multiple flow events, and it is possible the entire ridge volume was deposited in a single flow. In comparison to modern channels in the vicinity (3 m wide, 1 m deep), gravel-capped ridges have a ridge height that is at least twice the channel depth, and a maximum top width (1 m) that is two-thirds narrower than the channel width. We consider this size difference is an upper bound on the scale of the winnowing process for gravel-capped ridges. Another approach is to use the distance between gravels within the ridge deposit, which may approximate the minimum deflation length before a resistant lag starts to form. The maximum three-dimensional spacing of gravels (20 cm; Fig. 7) suggests that the gravel-capped ridges at this site have retained much of their original deposit volume. This line of reasoning implies the amount of ridge narrowing was perhaps only a ~30% reduction in ridge width relative to flow width.

5.4. Hydrologic environments associated with ridge types

Dated plant fragments from different inverted channel types have clustered ages that correspond to the broader reconstructed regional climatic trends. Therefore, the hydrologic environment was different when plants were present near the surface of the two ridge types (Fig. 15). The age dates suggest an association between key stages in the ridge formation and minor paleoclimate variations.

The ^{14}C dated wood for the gravel-capped ridges corresponds to the well-defined CAPE II wet period (Gayo et al., 2015; Santoro et al., 2017). Additional local organic specimens have similar radiometric dates corresponding to the CAPE II, including multiple dates between 12.8 and 11.7 kyr associated with human occupation in Quebrada Mani (Latorre et al., 2013), and one specimen from a lower elevation in Salar de Llamara dated to 12.8 kyr (Pfeiffer et al., 2018). In contrast, the remaining dates from our study are associated with arid periods. Wood samples from upper R4 correspond to the Mid-Holocene Dry Phase. The mudflow (MudX) age is during the Medieval Climate Anomaly.

Gravel-armored ridges are among the oldest surfaces at the study site (11–12.5 kyr), dating from a minor pluvial phase at the end of the Late Pleistocene into the Early Holocene (CAPE II). Sulfate-capped ridges are younger (8–9.5 kyr) and formed during a minor arid phase. Importantly, the radiometric age has different meanings for each ridge type. For gravel ridges, the age likely approximates the timing of flow. In contrast, the radiometric date at sulfate-capped ridge R4 corresponds to emplacement of the capping unit, which post-dated flow.

The differing planimetric patterns and sedimentology by ridge type suggest that connections are unlikely between the former flow channels now present as ridges. That is, the inverted channels were not all formerly part of the same flow event, but instead are exhumed from a laterally and vertically complex sedimentary deposit that formed over an extended period. However, we cannot rule out the possibility that both R4 and the gravel ridges had active

NASA Author Manuscript

NASA Author Manuscript

NASA Author Manuscript

flows during the same wet period (CAPE II), because there are indications of plant growth within the R4 section, but the timing is not well constrained (i.e., root casts are present, but there is insufficient dateable material). Dated wood associated with R4 is from the upper unit, from deposits interpreted to post-date flows within the channel. Thus, the R4 age dates obtained do not pinpoint the timing of flows, but rather indicate when evaporite formation occurred. Collectively, inverted channels at Salar de Llamara resulted from multiple episodes of surface overland flow and standing water spanning several thousand years.

In sum, we speculate that the key development stages that led to relief inversion appear to be tied to minor paleoclimate variations: gravel-bearing mudflows during slightly wetter periods and the sulfate capping unit formed in slightly drier conditions.

5.5. Implications for interpreting Martian inverted channels

On Mars, inverted channels are found on terrain spanning much of the planet's geologic history at sites across the globe (Williams, 2007; Dickson et al., 2021). The broad spatiotemporal distribution of these depositional systems can provide critical information on Martian paleoenvironments and by inference paleoclimate conditions. However, to place quantitative geologic constraints on the nature of Mars' climate change through study of inverted channels, a better understanding of their formative environments, the distinguishing attributes of inverted channel types, and the applicability of paleohydraulic models to inverted channels is needed.

Martian inverted channels are identified as extensive networks across intercrater plains (Burr et al., 2010; Davis et al., 2016; Di Pietro et al., 2018), on crater floor plains (Irwin III et al., 2018), and in association with multiple proposed and selected rover landing sites (e.g., Anderson and Bell, 2010; Irwin III et al., 2015; Palucis et al., 2014; Balme et al., 2020) including the *Perseverance* field site at Jezero crater (Goudge et al., 2018). The interpretation of Martian ridges as relict fluvial landforms is strengthened at sites with strong geologic context (e.g., Davis et al., 2019), but there are many locations where the origin of ridges is ambiguous or could be explained by alternate hypotheses such as structural features, dikes or eskers (e.g., Banks et al., 2009; Butcher et al., 2021). Even when there is broad consensus on a fluvial origin for some ridge networks, there remain disagreements in the interpretation of flow characteristics including magnitude and even flow direction (e.g., DiBiase et al., 2013; Lefort et al., 2015), which highlights the challenges in analysis of compound landscapes. Recent work has emphasized the importance of distinguishing inverted channels from exhumed channel belts on Mars (Cardenas et al., 2018; Hayden et al., 2019).

Of relevance to this study, Martian inverted channels are identified on hundreds of intracrater alluvial fans (Supplementary Fig. S9; Moore and Howard, 2005; Gullikson et al., 2016; Wilson et al., 2021). The close similarity of alluvial fans in the Atacama Desert to large-scale (tens of kms radial length) Martian alluvial fans, in terms of comparable scale, morphology, formative process and climatic setting, is detailed in Morgan et al. (2014). The PdT study site is also an important Mars analog due to the abundant sulfate minerals that are also prevalent on Mars (e.g., Gendrin et al., 2005; Bibring et al., 2006) and have been routinely detected by *Curiosity* instruments in Gale crater (Vaniman et al.,

NASA Author Manuscript NASA Author Manuscript NASA Author Manuscript

2018; Rampe et al., 2020). The PdT inverted channels serve as a cautionary example that inferences made from remotely sensed data without in situ outcrop observations may be a gross over-simplification of the system or incorrect. Through this study, we reach a better understanding of the capabilities and limitations for interpreting Martian inverted channels in similar settings, as well as their scientific value for in situ study. On this point, we discuss several specific inverted channel attributes:

1. *Planform*. There is a natural tendency to connect ridge segments in planetary mapping using orbital images (e.g., Di Pietro et al., 2018). However, considering the landscape as a 'snapshot' and linking inverted channel segments to define the former interconnected network may result in an inaccurate view of the depositional history. Rather, the PdT inverted channels are a time-integrated product of the alluvial system.

2. *Surface attributes*. The inverted channels' surface materials may not be identical to the original flow deposits. The PdT inverted channels illustrate grain size and compositional differences of the ridge surface relative to the original flow deposits. For the gravel-armoring case, there is a concentration of the coarsest fraction at the surface, an expected distortion of the original grain size distribution in the deposit caused by deflation. The sulfate-capped ridges highlight the possibility that fluvial sediment may be buried and, as in this case, overprinted by evaporites and sulfate plates.

3. *Induration mechanism*. Martian inverted channels are commonly located at the distal portions of fluvial systems (e.g., Davis et al., 2019), a geologic setting that could foster clast armoring or cementation. For most occurrences of Martian inverted channels, there is not an obvious connection to a volcanic source, and therefore lava-capping is considered a relatively rare induration mechanism. Williams et al. (2018) argue that the geologic setting and thermophysical characteristics of many of the larger inverted fluvial landforms on Mars are consistent with a cementation induration agent, rather than clast-armoring.

   With this study we document another mechanism for generating salt mineralogy associated with inverted channels; rather than cementing the fluvial deposits, chemical sedimentation was concentrated within the fluvial channel. As a result, the sulphate-capped inverted channels studied here would be compositionally indistinguishable from sulfate-cemented fluvial deposits in orbital visible and infrared spectral data.

   Two characteristics that could aid in differentiating cementation from clast armoring for Martian inverted channels are a) the time-varying thermal signature of the ridge, and b) the cross-sectional ridge shape. Preliminary studies in the Salar de Llamara show that the diurnal temperature response differs between these ridge types (Williams et al., 2018), a possible criterion to distinguish the capping material on Mars in thermal images. In terms of ridge shape, the PdT gravel-capped ridge has a rounded cross-sectional form. In contrast, a flat top (rectangular cross-section) is an attribute of the sulfate-capped ridges in this study, and has been recognized in cemented fluvial deposits elsewhere (e.g.,

NASA Author Manuscript NASA Author Manuscript NASA Author Manuscript

Williams et al., 2009; Clarke et al., 2020). To delineate this shape distinction for the PdT ridges requires high resolution topographic data (<0.25 m/pix) or in situ observations.

4. *Paleoflow dimensions*. Multiple studies have estimated paleoflow conditions for Martian inverted channels using the ridge dimensions as a proxy for flow channel dimensions (e.g., Burr et al., 2010; Williams et al., 2009, 2013; Palucis et al., 2014; Kite et al., 2015). Researchers acknowledge that the uncertainty in this approach can lead to an overestimation (e.g., if the relief inversion is a channel belt) or underestimation (e.g., if the ridge side slopes have retreated) of the flow paleohydraulics (e.g., Williams et al., 2009; Hayden et al., 2019). This uncertainty can be better quantified by understanding the various settings for 1) the correlation between ridge width and height to flow dimensions, 2) the factors that alter ridge dimensions, and 3) attributes that aid in characterizing the geologic setting. Where there are well-preserved meanders, such as at Eberswalde and Aeolis Dorsa, the measured ridge width is consistent with the meander geometry (e.g., Moore et al., 2003; Burr et al., 2010). However, this is uncommon; the vast majority of Martian inverted channels have formed in aggradational settings with channel switching rather than lateral migration (termed deposit inversion by DiBiase et al. (2013), and differs from the landscape inversion examples highlighted in this study).

   In this study, the different formation histories of the inverted channel types have bearing on the degree of preservation of original flow dimension. The sulfate-capped ridge had minimal lateral reduction from the original channel width, whereas ~70% or more of the flow width is probably preserved in the widest reaches of gravel-capped ridges. This small reduction in width appears to be tied to the erosive environment: dominantly aeolian deflation in the absence of significant runoff or aggressive slope processes in a hyperarid climate. For these two ridge types, the greatest uncertainty is in estimating paleoflow depth from ridge dimensions. The ridge height does not bear a consistent or predictable relationship to the paleoflow depth: only the top third of the sulfate-capped ridge is associated with the fluvial phase of its history, whereas the gravel-capped ridges could reflect a single flow deposit where a streamflow origin is confirmed or assumed, the flow conditions can be estimated to within an order of magnitude, consistent with other studies that accounted for the specific fluvial environment and adopted reasonable boundary conditions (e.g., Williams et al., 2009; Morgan and Craddock, 2019).

5. *Biosignature potential*. Fluvial deposits are recognized as a moderate potential biosignature repository on Mars, due to the possibility of water-transported organics (Summons et al., 2011). Less appreciated is the role of biosignatures that may form in situ for Martian fluvial environments. This study highlights a candidate microenvironment for habitability and potential biosignature preservation within a fluvial conduit: the sulfate domes and discs atop the R4/R5 ridges. Although the role of microbialites in gypsum dome formation is unknown, Rasuk et al. (2014) documented an array of associated biosignatures

NASA Author Manuscript

NASA Author Manuscript

NASA Author Manuscript

(e.g., extracellular polymeric substances, organic matter, or bacteria coated in amorphous gypsum) within these sulfates, substantiating that endoevaporities have good preservation potential for signs of life. If similar sulfate plates are associated with fluvial deposits on Mars, such specimens would be scientifically valuable for sample return.

6. Conclusions

Through age-dated samples and characterization of ridge sedimentology, mineralogy, and morphology, we identify links between environmental conditions and the evolutionary sequence for the PdT inverted channels. The Salar de Llamara inverted channels preserve a compound aqueous history spanning several thousand years, with episodic surface flows, and a fluctuating water table (groundwater precipitation and alteration) contributing to ridge development over cycles of wet and dry periods. We find that two mechanisms lead to differential aeolian erosion and channel inversion: gravel armoring with very minor local lithification, and evaporite infilling, a previously unrecognized process. These two types of inverted channels are in close proximity and apparently record minor variations in paleoclimate conditions. During CAPE II, distributary channels on the alluvial fan had gravel-bearing mudflows. In a subsequent minor arid phase, evaporite deposition occurred in pre-existing fluvially-carved, contributory channels on the distal alluvial fan. Wind-driven deflation (erosion rate > 0.1–0.2 m/kyr) produced ridge landforms in both cases, albeit exploiting different depositional processes. The two types of ridges—gravel-capped and sulfate-capped—are an example of equifinality.

Likewise on Mars, inverted channels may preserve a complex aqueous history. Investigations of Martian inverted channels that rely on orbital data can yield a general reconstruction but are subject to uncertainties and limitations. Outcrop to grain-scale observations are needed to accurately constrain the process, flow magnitude, historical sequence of events, and paleoclimate context.

Supplementary Material

Refer to Web version on PubMed Central for supplementary material.

Acknowledgments

This research was supported by grants to R.M.E. Williams from the NASA Mars Fundamental Research Program (NNX13AG83G) and the NASA Mars Data Analysis Program (80NSSC19K1216). The authors thank Dr. David Blake (NASA-Ames) for use of the Olympus Terra XRD during multiple field campaigns. Wood samples were analyzed at the National Ocean Sciences Accelerator Mass Spectrometer (NOSAMS) facility which is supported through NSF Cooperative Agreement #OCE-1239667. We are grateful to Dr. Michael Malin for constructive critique of this work as well as for the time and effort of the reviewers: Dr. Joel Davis (Natural History Museum, UK), Dr. Colin Pain (University of Sevilla), and an anonymous reviewer. We appreciate the assistance of Dr. Jan Schween (University of Cologne) in obtaining weather station data. Image data used in this study are archived with the Planetary Data Systems for Mars data sets, and Earth images can be viewed via Google Earth. Data supporting the conclusions presented are available in the figures, tables, and supplementary information.

NASA Author Manuscript NASA Author Manuscript NASA Author Manuscript

References

Alpers CN, Brimhall GH, 1988. Middle Miocene climatic change in the Atacama Desert, northern Chile: evidence from supergene mineralization at La Escondia. Geol. Soc. Am. Bull 100, 1640–1656. 10.1130/0016-7606(1988)1002.3.CO;2.

Amundson R, Dietrich WE, Bellugi D, Ewing S, Nishiizumi K, Guillermo C, Owen J, Finkel R, Heimsath A, Stewart B, Caffee M, 2012. Geomorphologic evidence for the late Pliocene onset of hyperaridity in the Atacama Desert. Geol. Soc. Am. Bull 124 (7–8), 1048–1070. 10.1130/B30445.1.

Anderson RB, Bell JF, 2010. Geologic mapping and characterization of Gale Crater and implications for its potential as a Mars Science Laboratory landing site. Mars 5, 76–128. 10.1555/mars.2010.0004.

Aref M, 2003. Classification and depositional environments of Quaternary pedogenic gypsum crusts (gypcrete) from east of the Fayum Depression, Egypt. Sediment. Geol 155 (1–2), 87–108. 10.1016/S0037-0738(02)00162-8.

Azam S, 2007. Study on the geological and engineering aspects of anhydrite/gypsum transition in the Arabian Gulf coastal deposits. Bull. Eng. Geol. Environ 66, 177–185. 10.1007/s10064-006-0053-2.

Azimi G, Papangelakis VG, 2011. Mechanism and kinetics of gypsum–anhydrite transformation in aqueous electrolyte solutions. Hydrometallurgy 108 (1–2), 122–129. 10.1016/j.hydromet.2011.03.007.

Balme MRS, Davis JM, Fawdon P, Grindrod PM, Bridges JC, Sefton-Nash E, Williams RME, 2020. Aram dorsum: an extensive Noachian-age fluvial depositional system in Arabia Terra, Mars. J. Geophys. Res 125 (5). 10.1029/2019JE006244 32 pp.

Betancourt JL, Latorre C, Rech JA, Quade J, Rylander KA, 2000. A 22,000-year record of monsoonal precipitation from Northern Chile's Atacama Desert. Science 289 (5484), 1542–1546. 10.1126/science.289.5484.1542. [PubMed: 10968788]

Bibring JP, et al. , 2006. Global mineralogical and aqueous Mars history derived from OMEGA/Mars Express data. Science 312, 400–404. 10.1126/science.1122659. [PubMed: 16627738]

Blake D, et al. , 2012. Characterization and calibration of the CheMin mineralogical instrument on Mars Science Laboratory. Space Sci. Rev 170 (1–4), 341–399. 10.1007/s11214-012-9905-1.

Banks ME, Lang NP, Kargel JS, McEwen AS, Baker VR, Grant JA, Pelletier JD, Strom RG, 2009. An analysis of the Sinuous Ridges in the Southern Argyre Planitia, Mars using HiRISE and CTX Images and MOLA data. J. Geophys. Res 14 (E09003), 19. 10.1029/2008JE003244.

Buffington JM, Montgomery DR, 1999. A procedure for classifying and mapping textural facies in gravel-bed rivers. Water Resour. Res 35 (6), 1903–1914. 10.1029/1999WR900041.

Bunte K, Abt SR, 2001. Sampling surface and subsurface particle-size distributions in wadable gravel-and cobble-bed streams for analyses in sediment transport, hydraulics, and streambed monitoring. U.S. Department of Agriculture General Technical Report RMRS-GTR-74 10.2737/RMRS-GTR-74 428 pp.

Burr DM, Williams RME, Chojnacki M, Wendell KD, Emery JP, 2010. Inverted fluvial features in the Aeolis/Zephyria Plana region, Mars: formation mechanism and initial paleodischarge estimates. J. Geophys. Res 115 (E07011). 10.1029/2009JE003496 20 pp.

Butcher FE, Balme MR, Conway SJ, Gallagher C, Arnold NS, Storrar RD, Lewis SR, Hagermann A, Davis JM, 2021. Sinuous ridges in Chukhung Crater, Tempe Terra, Mars: implications for fluvial, glacial, and glaciofluvial activity. Icarus 357 (114131), 27. 10.1016/j.icarus.2020.114131.

Cardenas BT, Mohrig D, Goudge TA, 2018. Fluvial stratigraphy of valley fills at Aeolis Dorsa, Mars: evidence for base-level fluctuations controlled by a downstream water bod. GSA Bull. 130 (3–4), 484–498. 10.1130/B31567.1.

Charrier R, Pinto MP Rodriquez MP, 2007. Chapter 3: Tectonostratigraphic evolution of the Andean Orogen in Chile. In: Moreno T, Gibbons W (Eds.), The Geology of Chile. Geological Society of London 10.1144/GOCH.3.

Chong G, López PL, Luis F, Auqué LF, Garcés I, 1999. Características geoquímicas y pautas deevolución de las salmueras superficiales del Salar de Llamara, Chile. Rev. Geol. Chile 26 (1), 89–108.

NASA Author Manuscript NASA Author Manuscript NASA Author Manuscript

Clarke JDA, 2006. Antiquity of aridity in the Chilean Atacama Desert. Geomorphology 73 (1–2), 101–114. 10.1016/j.geomorph.2005.06.008.

Clarke JDA, Pain CF, Rupert S, 2020. Complex expressions of inverted and exhumed relief in central Utah, and some martian counterparts. Phys. Geogr 10.1080/02723646.2020.1839161 18. pp.

Davis JM, Balme MR, Grindrod PM, Williams RME, Gupta S, 2016. Extensive Noachian fluvial systems in Arabia Terra: implications for early martian climate. Geology 44 (10), 879–880. 10.1130/G38247.1.

Davis JM, Gupta S, Balme MR, Grindrod PM, Fawdon P, Gupta S, Dickeson ZI, Williams RME, 2019. A diverse array of fluvial depositional systems in Arabia Terra: evidence for mid-Noachian to early Hesperian rivers on Mars. J. Geophys. Res 124 (7), 1913–1934. 10.1029/2019JE005976.

Di Pietro I, Ori GG, Pondrelli M, Salese F, 2018. Geology of Aeolis Dorsa alluvial sedimentary basin, Mars. J. Maps 14 (2), 212–218. 10.1080/17445647.2018.1454350.

DiBiase RA, Limaye AB, Scheingross JS, Fischer WW, Lamb MP, 2013. Deltaic deposits at Aeolis Dorsa: sedimentary evidence for a large body of water in the northern plains of Mars. J. Geophys. Res 118 (6), 1–18. 10.1002/jgre.20100.

Dickson JL, Lamb MP, Williams RME, Hayden AT, Fischer WW, 2021. The global distribution of depositional rivers on early Mars. Geology 49 (5), 504–509. 10.1130/G48457.1.

Dietrich WE, Palucis MC, Williams RME, Leis KW, Rivera-Hernandez F, Sumner DY, 2017. Chapter 28. Fluvial gravels on Mars: analysis and implications. In: Tsutsumi D, Laronne J (Eds.), Gravel Bed Rivers: Processes and Disasters. Wiley, pp. 755–776 10.1002/9781118971437.

Dingman RJ, Galli CO, 1965. Geology and ground-water resources of the Pica area, Tarapaca Province, Chile. U. S. Geological Survey Bulletin No. 1189 10.3133/b1189 122 pp. http://pubs.er.usgs.gov/publication/b1189.

Dunai TJ, Gonzalez-Lopez GA, Juez-Larre J, Carrizo D, 2005. Oligocene/Miocene age of aridity in the Atacama Desert revealed by exposure dating of erosion sensitive landforms. Geology 33 (4), 321–324. 10.1130/G21184.1.

Ericksen GE, 1981. Geology and origin of the Chilean nitrate deposits. U. S. Geological Survey Professional Paper 1188, p. 51 10.3133/pp1188.

Evenstar LA, Hartley AJ, Stuart FM, Mather AE, Rice CM, Chong G, 2009. Multi-phase development of the Atacama Planation Surface recorded by cosmogenic ^{3}He exposure ages: Implications for uplift and Cenozoic climate change in western South America. Geology 37 (1), 27–30. 10.1130/G25437A.1.

Evenstar LA, Mather AE, Hartley AJ, Stuart FM, Sparks RSJ, Cooper FJ, 2017. Geomorphology on geologic timescales: evolution of the late Cenozoic Pacific paleosurface in Northern Chile and Southern Peru. Earth Sci. Rev 171, 1–27. 10.1016/j.earscirev.2017.04.004.

Evenstar LA, Hartley AJ, Mather AE, 2020. Using spatial patterns of fluvial incision to constrain continental-scale uplift in the Andes. Glob. Planet. Chang 186 (103119), 186. 10.1016/j.gloplacha.2020.103119.

Farías ME, Charrier D, Comte J, Martinod J, Herail G, 2005. Late Cenozoic deformation and uplift of the western flank of the Altiplano: evidence from the depositional, tectonic, and geomorphologic evolution and shallow seismic activity (northern Chile at 19°30′S). Tectonics 24 (TC4001), 29. 10.1029/2004TC001667.

Finstad KM, Pfeiffer M, McNicol G, Barnes JW, Demergasso C, Chong G, Amundson R, 2016. Rates and geochemical processes of soil and salt crust formation in Salars of the Atacama Desert, Chile. Geoderma 284, 57–72. 10.1016/j.geoderma.2016.08.020.

Foix N, et al. , 2012. Fluvial styles, palaeohydrology and modern analogues of an exhumed, Cretaceous fluvial system: Cerro Barcino Formation, Cañadón Asfalto Basin, Argentina. Cretaceous Res. 34, 298–307. 10.1016/j.cretres.2011.11.010.

Friend PF, Slater MJ, Williams RC, 1979. Vertical and lateral building of river sandstone bodies, Ebro Basin, Spain. J. Geol. Soc 136 (1), 39–46. 10.1144/gsjgs.136.1.0039.

Galli C, Dingman I, 1962. Cuadrángulos Pica, Alca, Matilla y Chacarilla, con un estudio sobre los recursos de agua subterránea, Provincia de Tarapacá, Scale 1:50.000. Carta Geol. Chile 3 (125 pp).

NASA Author Manuscript NASA Author Manuscript NASA Author Manuscript

Gayo EM, Loatorre C, Jordan TE, Nester PL, Estay SA, Ojeda KF, Santoro CM, 2012. Late Quaternary hydrological and ecological changes in the hyperarid core of the northern Atacama Desert (~21°S). Earth Sci. Rev 113, 120–140. 10.1016/j.earscirev.2012.04.003.

Gayo EM, Latorre C, Santoro CM, 2015. Timing of occupation and regional settlement patterns revealed by time-series analyses of an archaeological radiocarbon database for the South-Central Andes (16°–25°S). Quat. Int 356, 4–14. 10.1016/j.quaint.2014.09.076.

Gendrin A, et al. , 2005. Sulfates in the martian layered terrains: the OMEGA/Mars Express View. Science 307 (5715), 1587–1591. 10.1126/science.1109087. [PubMed: 15718429]

González LG, Dunai T, Carrizo D, Allmendinger R, 2006. Young displacements on the Atacama Fault System, northern Chile from field observations and cosmogenic ^{21}Ne concentrations. Tectonics 25 (3), 15. 10.1029/2005TC001846.

Google Earth, 2013. version 7.1.2.2041, Images Near 21° 16.123′ S, 69° 37.088′ W (Image credit: earth.google.com/web/. Satellite image date: 12/11/2006. Accessed May 17, 2020).

Goudge TA, Mohrig D, Cardenas BT, Hughes CM, Fassett CI, 2018. Stratigraphy and paleohydrology of delta channel deposits, Jezero crater, Mars. Icarus 301, 58–75. 10.1016/j.icarus.2017.09.034.

Gullikson AL, Anderson RB, Williams RME, 2016. Mapping Sinuous Ridges in Northwest Hellas, Mars: Houston, Texas, Lunar and Planetary Science Conference XLVII, Abstract #2376.

Hardie LA, 1967. The gypsum-anhydrite equilibrium at one atmosphere pressure. Am. Mineral 52 (1–2), 171–200.

Hartley AJ, Evenstar LA, 2010. Ceonzoic stratigraphic development in the north Chilean forearc: implications for basin development and uplift history of the Central Andean margin. Tectnophysics 495, 67–77. 10.1016/j.tecto.2009.05.013.

Hartley AJ, Mather AE, Jolley Turner, P., 2005. Climatic controls on alluvial fan activity, coastal Cordillera, northern Chile. Alluvial Fans: Geomorphology, Sedimentology, Dynamics. Special Publications Geological Society of Londonv. 251. Geological Society of London, pp. 95–115. 10.1144/GSL.SP.2005.251.01.08.

Harvey AM, 2011. Dryland alluvial fans. In: Thomas DSG(Ed.), Arid Zone Geomorphology: Process, Form and Change in Drylands, Third edition John Wiley & Sons, Hoboken, NJ, pp. 333–371 10.1002/9780470710777.ch14.

Haug EW, Kraal ER, Sewall JO, Van Dijk M, Diaz G, 2010. Climatic and geomorphic interactions on alluvial fans in the Atacama Desert, Chile. Geomorphology 121, 184–196. 10.1016/j.geomorph.2010.04.005.

Hayden AT, McElroy BJ, Lamb MP, Williams RME, Ewing RC, Fischer WW, 2019. Formation of sinuous ridges by inversion of river-channel belts on Earth and Mars. Icarus 332 (1), 92–110. 10.1016/j.icarus.2019.04.019.

Hoffmeister D, 2017. Meteorological and soil measurements of the permanent basic weather station 14 - Salar de Llamara, Chile. CRC1211 Database (CRC1211DB) 10.5880/CRC1211DB.5.

Hogg AG, et al. , 2013. SHCal13 southern hemisphere calibration, 0–50,000 years cal BP. Radiocarbon 55 (4), 1889–1903. 10.2458/azu_js_rc.55.

Hoke GD, Isacks BL, Jordan TE, Blanco N, Tomlinson AJ, Ramezani J, 2007. Geomorphic evidence for post-10 Ma uplift of the western flank of the central Andes 18°30′–22°S. Tectonics 26, 17. 10.1029/2006TC002082.

Houston J, 2002. Groundwater recharge through an alluvial fan in the Atacama Desert, northern Chile: mechanisms, magnitudes and causes. Hydrol. Process 16, 3019–3035. 10.1002/hyp.1086.

Houston J, 2009. A recharge model for high altitude, arid, Andrean aquifers. Hydrol. Process 330, 402–412. 10.1002/hyp.7350.

Houston J, Hart D, 2004. Theoretical head decay in closed basin aquifers: an insight into fossil groundwater and recharge events in the Andes of northern Chile. Quaternary J. Eng. Geol. Hydrol 37, 131–139. 10.1144/1470-9236/04-007.

Houston J, Hartley A, 2003. The central Andean west-slope rainshadow and it potential contribution to the origin of the hyper-aridity in the Atacama desert. Int. J. Climatol 23, 1453–1464. 10.1002/joc.938.

Howard AD, Dietrich WE, Williams RME, Morgan AM, Irwin III RP, Moore JM, 2016. Mudflow alluvial fans of the Atacama Desert in Chile. Geol. Soc. Am. Abstr. Prog

NASA Author Manuscript NASA Author Manuscript NASA Author Manuscript

48 (7). 10.1130/abs/2016AM-283742 abstract #283742. https://gsa.confex.com/gsa/2016AM/webprogram/Paper283742.html.

Huang W, Ertekin E, Wang T, Cruz L, Dailey M, Diruggiero J, Kisailus D, 2020. Mechanism of water extraction from gypsum rock by desert colonizing microorganisms. Proc. Natl. Acad. Sci 117 (20), 10681–10687. 10.1073/pnas.2001613117. [PubMed: 32366642]

Irwin RP III, Lewis KW, Howard AD, Grant JA, 2015. Paleohydrology of Eberswalde Crater, Mars. Geomorphology 240, 83–101. 10.1016/j.geomorph.2014.10.012.

Irwin RP III, Wray JJ, Mest SC, Maxwell TA, 2018. Wind-eroded crater floors and intercrater plains, Terra Sabaea, Mars. J. Geophys. Res 123 (2), 445–467. 10.1002/2017JE005270.

Izquierdo T, Abad M, Bernardez E, 2016. Catastrophic flooding caused by a mudflow in the urban area of Copiapó (Atacama Desert, northern Chile). Lisbon, Portugal, International Conference on Urban Risks, 30 June–2 July 2016.

Jayne RS, Pollyea RM, Dodd JP, Olson EJ, Swanson SK, 2016. Spatial and temporal constraints on regional-scale groundwater flow in the Pampa del Tamarugal Basin, Atacama Desert, Chile. Hydrogeol. J 24 (8), 1921–1937. 10.1007/s10040-016-1454-3.

Jordan TE, Kirk-Lawlor NE, Blanco NP, Rech JA, Cosentino NJ, 2014. Landscape modification in response to repeated onset of hyperarid paleoclimate states since 14 Ma, Atacama Desert, Chile. Geol. Soc. Am. Bull 126 (7/8), 1016–1046. 10.1130/B30978.1.

Kiefer E, Dörr MJ, Ibbeken H, Götze HJ, 1997. Gravity-based mass balance of an alluvial fan giant: the Arcas Fan, Pampa del Tamarugal, northern Chile. Rev. Geol. Chile 24, 165–185. 10.5027/andgeoV24n2-a03.

Kite ES, Howard AD, Lucas A, 2015. Resolving the era of river-forming climates on Mars using stratigraphic logs of river-deposit dimensions. Earth Planet. Sci. Lett 420, 55–65. 10.1016/j.epsl.2015.03.019.

Knight DW, Demetriou JD, Homed ME, 1984. Boundary shear in smooth rectangular channels. Agric. Water Manag 110 (4), 405–422. 10.1061/(ASCE)0733-9429(1984)110:4(405).

Kokaly RF, et al., 2017. USGS Spectral Library Version 7 Data: U.S. Geological Survey Data Release, Data Series 1035. 10.5066/F7RR1WDJ available at. https://pubs.er.usgs.gov/publication/ds1035.

Labbé N, García M, Simicic Y, Contreras-Reyes E, Charrier R, Pascale GD, Arriagada C, 2019. Sediment fill geometry and structural control of the Pampa del Tamarugal basin, northern Chile. GSA Bull. 131 (1–2), 155–174. 10.1016/10.1130/B31722.1.

Latorre C, Betancourt JL, Rylander KA, Quade J, Matthei O, 2003. A vegetation history from the arid prepuna of northern Chile (22–23°S) over the last 13,500 years. Palaeogeogr. Palaeoclimatol. Palaeoecol 194, 223–246. 10.1016/s0031-0182(03)00279-7.

Latorre C, Santoro CM, Ugalde PC, Gayo EM, Osorio D, Salas-Egaña C, De Pol-Holz R, Joly D, Rech JA, 2013. Late Pleistocene human occupation of the hyperarid core in the Atacama Desert, northern Chile. Quat. Sci. Rev 77, 19–30. 10.1016/j.quascirev.2013.06.008.

Lefort A, Burr DM, Nimmo F, Jacobsen RE, 2015. Channel slope reversal near the Martian dichotomy boundary: testing tectonic hypotheses. Geomorphology 240, 121–136. 10.1016/j.geomorph.2014.09.028.

Maizels J, 1990. Raised channel systems as indicators or palaeohydrologic change: a case study from Oman. Palaeogeogr. Palaeoclimatol. Palaeoecol 76, 241–277. 10.1016/0031-0182(90)90115-N.

Marker M, Dangel F, Bauerle MVS, Rodolfi G, 2012. Assessment of natural hazards and vulnerability in the Rio Copiapó Catchment: a case study in the ungauged Quebrada Cinchado Catchment. Investig. Geogr. Chile 44, 17–28.

Mather AE, Hartley A, 2005. Flow events on a hyper-arid alluvial fan: Quebrada Tambores, Salar de Atacama, northern Chile. In: Harvey AM, Mather AE, Stokes M (Eds.), Alluvial Fans: Geomorphology, Sedimentology, Dynamics. v. 251. Geological Society, London, pp. 9–29. 10.1144/GSL.SP.2005.251.01.01.

McFadden LD, Wells SG, Jercinovich MJ, 1987. Influences of eolian and pedogenic processes on the origin and evolution of desert pavements. Geology 15, 504–508. 10.1016/0341-8162(92)90018-7.

Miller DM, Dudash SL, McGeehin JP, 2018. Paleoclimate record for Lake Coyote, California, and the Last Glacial Maximum and deglacial paleohydrology (25 to 14 cal ka) of the Mojave River. In: Starratt SW, Rosen MR (Eds.), From Saline to Freshwater: The Diversity of Western

NASA Author Manuscript NASA Author Manuscript NASA Author Manuscript

Lakes in Space and Time. Geological Society of America Special Paper 536, pp. 1–20 10.1130/2018.2536(12)

Boulder, Co. Moore JM, Howard AD, 2005. Large alluvial fans on Mars. J. Geophys. Res 110 (E04005). 10.1029/2004JE002352.

Moore JM, Howard AD, Dietrich WE, Schenk PM, 2003. Martian layered fluvial deposits: implications for Noachian climate scenarios. Geophys. Res. Lett 30 (24), 2292. 10.1029/2003GL019002.

Morgan AM, Craddock RA, 2019. Assessing the accuracy of paleodischarge estimates for rivers on Mars. Geophys. Res. Lett 46 (21), 11738–11746. 10.1029/2019GL084921.

Morgan AM, Howard AD, Hobley DE, Moore JM, Dietrich WE, Williams RME, Burr DM, Grant JA, Wilson SA, Matsubara Y, 2014. Sedimentology and climatic environment of alluvial fans in the Martian Saheki crater and a comparison with terrestrial fans. Icarus 229, 131–156. 10.1016/j.icarus.2013.11.007.

Mortimer C, Ferrar TE, Saric N, 1974. K-Ar ages from Tertiary lavas of the northern-most Chilean Andes. Geol. Rundsch 63, 484–490.

Muñoz RC, Falvey MJ, Arancibia M, Astudillo VI, Elgueta J, Ibarra M, Santana C, Vasquez C, 2018. Wind energy exploration over the Atacama Desert: a numerical model–guided observational program. Am. Meteorol. Soc 99, 2079–2092. 10.1175/BAMS-D-17-0019.1.

Nester PL, Jordan T, 2011. Chapter 18. The Pampa del Tamarugal forearc basin in Northern Chile: the interaction of tectonics and climate. In: Busby C, Azor A (Eds.), Tectonics of Sedimentary Basins: Recent Advances. Blackwell Publishing Ltd, Hoboken, NJ, pp. 369–381 10.1002/9781444347166.ch18.

Nester PL, Gayo E, Latorre C, Jordan TE, Blanco N, 2007. Perennial stream discharge in the hyperarid Atacama Desert of northern Chile during the latest Pleistocene. Proc. Natl. Acad. Sci 104 (50), 19724–19729. 10.1073/pnas.0705373104. [PubMed: 18056645]

Niem AR, 1974. Wright's Point, Harney County, Oregon, an example of inverted topography. Ore Bin 36, 33–49.

Nishiizumi K, Caffee MW, Finkel RC, Brimhall G, Mote T, 2005. Remnants of a fossil alluvial fan landscape of Miocene age in the Atacama Desert of northern Chile using cosmogenic nuclide exposure age dating. Earth Planet. Sci. Lett 237, 499–507. 10.1016/j.epsl.2005.05.032.

Noe Dobrea E, Williams RME, Howard AD, Dietrich W, Irwin RP, 2017. Mineralogy of a cemented inverted channel, Atacama, Chile: clues to its formation. Geol. Soc. Am. Abstr. Prog 49 (6). 10.1130/abs/2017AM-307834 abstract #307834.

Pain CF, Ollier CD, 1995. Inversion of relief—a component of landscape evolution. Geomorphology 12, 151–165. 10.1016/0169-555X(94)00084-5.

Palucis MC, Dietrich WE, Hayes AG, Williams RME, Sumner DY, Hardgrove C, Gupta S, Calef FJ III, 2014. The origin and evolution of the Peace Vallis fan system that drains to the Curiosity landing area, Gale Crater. J. Geophys. Res 119 (4), 705–728. 10.1002/2013JE004583.

Pfeiffer M, et al. , 2018. Chronology, stratigraphy and hydrological modelling of extensive wetlands and paleolakes in the hyperarid core of the Atacama Desert during the late quaternary. J. Geophys. Res 119 (4), 705–728. 10.1016/j.quascirev.2018.08.001.

Pfeiffer M, Morgan AM, Heimsath A, Jordan T, Howard AD, Amundson R, 2021. Century scale rainfall in the absolute Atacama Desert: landscape response and implications for past and future rainfall. Quaternary Sci. Rev, 254 10.1016/j.quascirev.2021.106797.

Pueyo JJ, Chong G, Jensen A, 2001. Neogene evaporites in desert volcanic environments: Atacama Desert, northern Chile. Sedimentology 48 (6), 1411–1431. 10.1046/j.1365-3091.2001.00428.x.

Quang CX, Clark AH, Lee JKW, 2005. Response of supergene processes to episodic Cenozoic uplift, pediment erosion, and ignimbrite eruption in the porphyry copper province of southern Perú. Econ. Geol 100, 87–114. 10.2113/100.1.0087.

Quezada AJ, Vasquez P, Sepulveda F, 2012. Mapa Compilacion Geologica Area Quillagua—Alar Grande, Region De Tarapaca: Chilean National Geology Branch (scale 1:100,000).

Rampe EB, et al. , 2020. Mineralogy and geochemistry of sedimentary rocks and eolian sediments in Gale crater, Mars: a review after six Earth years of exploration with Curiosity. Geochemistry 80 (2). 10.1016/j.chemer.2020.125605.

NASA Author Manuscript NASA Author Manuscript NASA Author Manuscript

Rasuk MC, Kurth D, Flores MR, Contreras M, Novoa F, Poire D, Farías ME, 2014. Microbial characterization of microbial ecosystems associated to evaporites domes of gypsum in Salar de Llamara in Atacama Desert. Microb. Ecol 68 (3), 483–494. 10.1007/s00248-014-0431-4. [PubMed: 24859438]

Rech JA, Quade J, Betancourt JL, 2002. Late Quaternary paleohydrology of the central Atacama Desert (lat 22°–24°S), Chile. Geol. Soc. Am. Bull 114 (3), 334–348. 10.1130/0016-7606(2002)114<0334:LQPOTC>2.0.CO;2.

Rech JA, Quade J, Hart WS, 2003. Isotopic evidence for the source of Ca and S in soil gypsum, anhydrite and calcite in the Atacama Desert, Chile. Geochim. Cosmochim. Acta 67 (4). 10.1016/S0016-7037(02)01175-4.

Rech JA, Currie BS, Michalski G, Cowan AM, 2006. Neogene climate change and uplift in the Atacama Desert, Chile. Geology 34, 761–764. 10.1130/G22444.1.

Ritter B, Binnie SA, Stuart FM, Wennrich V, Dunai T, 2018a. Evidence for multiple Plio-Pleistocene lake episodes in the hyperarid Atacama Desert. Quat. Geochronol 44, 1–12. 10.1016/j.quageo.2017.11.002.

Ritter B, Stuart FMFM, Binnioe SASA, Gendes A, Wennrich V, Dunai TJTJ, 2018b. Neogene fluvial landscape evolution in the hyperarid core of the Atacama Desert. Sci. Rep 8 (13952). 10.1038/s41598-018-32339-9 16 pp. [PubMed: 29311647]

Ritter B, Wennrich V, Medialdea A, Brill D, King G, Schneiderwind S, Niemann K, FernÃ¡ndez-Galego E, Diederich J, Rolf C, Bao R, Melles M, Dunai TJ, 2019. Climatic fluctuations in the hyperarid core of the Atacama Desert during the past 215 ka. Scient. Rep 9 (1), 5270. 10.1038/s41598-019-41743-8.

Saez A, Cabrera L, Jensen A, Chong G, 1999. Late Neogene lacustrine record and palaeogeography in the Quillagua–Llamara basin, Central Andean fore-arc (northern Chile). Palaeogeogr. Palaeoclimatol. Palaeecol 151, 5–37. 10.1144/0016-76492007-022.

Santoro CM, et al. , 2017. Continuities and discontinuities in the socio-environmental systems of the Atacama Desert during the last 13,000 years. J. Anthropol. Archaeol 46, 28–39. 10.1016/j.jaa.2016.08.006.

Scheihing KW, 2018. Evidence of short-term groundwater recharge signal propagation from the Andes to the central Atacama Desert: a singular spectrum analysis approach. Hydrol. Sci. J 63 (8), 1255–1261. 10.1080/02626667.2018.1495838.

Stoertz GE, Ericksen GE, 1974. Geology of salars in northern Chile. U. S. Geological Survey Professional Paper 811, pp. 1–65 10.3133/pp811.

Stuiver M, Reimer PJ, Reimer RW, 2019. CALIB 7.1. http://calib.org. (Accessed July 2019).

Summons RE, Amend JP, Bish D, Buick R, Cody GD, Marais DJD, Dromart G, Eigenbrode JL, Knoll AH, Sumner DY, 2011. Preservation of Martian organic and environmental records: final report of the Mars Biosignature Working Group. Astrobiology 11 (2), 157–181. 10.1089/ast.2010.0506. [PubMed: 21417945]

Vaniman DT, et al. , 2018. Gypsum, bassanite, and anhydrite at Gale crater, Mars. Am. Mineral 103 (7), 1011–1020. 10.2138/am-2018-6346.

Voigt C, Klipsch S, Herwartz D, Chong G, Staubwasser M, 2020. The spatial distribution of soluble salts in the surface soil of the Atacama Desert and their relationship to hyperaridity. Glob. Planet. Chang, 184 10.1016/j.gloplacha.2019.103077.

Warren JK, 2016. Evaporites: A Geological Compendium. Springer, Cham 10.1007/978-3-319-13512-0_1 1657 pp.

Watson, 1988. Desert gypsum crusts as palaeoenvironmental indicators: a micropetrographic study of crusts from southern Tunisia and the central Namib Desert. J. Arid Environ 15 (1), 19–42. 10.1016/S0140-1963(18)31002-4.

Wilcox AC, Escauriaza C, Agredano R, Mignot E, Zuazo V, Otarola S, Castro L, Gironas J, Cienfuegos R, Mao L, 2016. An integrated analysis of the March 2015 Atacama floods. Geophys. Res. Lett 43. 10.1002/2016GL069751 9 pp.

Williams RME, 2007. Global Spatial Distribution of Raised Curvilinear Features on Mars: Houston, Texas, Lunar and Planetary Science Conference XXXVIII (abstract 1821).

NASA Author Manuscript NASA Author Manuscript NASA Author Manuscript

Williams RME, Irwin RP III, Zimbelman JR, 2009. Evaluation of paleohydrologic models for terrestrial inverted channels: implications for application to Martian sinuous ridges. Geomorphology 107, 300–315. 10.1016/j.geomorph.2008.12.015.

Williams RME, Irwin RP III, Zimbelman JR, Chidsey TC Jr., Eby DE, 2011. Field guide to exhumed paleochannels near Green River, Utah: terrestrial analogs for sinuous ridges on Mars. In: Garry WB, Bleacher J (Eds.), Geological Society of America Special Paper 483: Analogs for Planetary Exploration. Geological Society of America, pp. 483–506 10.1130/2011.2483(29).

Williams RME, Irwin RPI, Burr DM, Harrison T, McClelland P, 2013. Variability in Martian Sinuous Ridge Form: case study of Aeolis Serpens in the Aeolis Dorsa, Mars, and insight from the Mirackina Paleoriver, South Australia. Icarus 225 (1), 308–324. 10.1016/j.icarus.2013.03.016.

Williams RME, Chuang FC, Berman DC, 2017. Multiple surface wetting events in the greater Meridiani Planum Region, Mars: evidence from valley networks within ancient cratered highlands. Geophys. Res. Lett 44 (4), 1669–1678. 10.1002/2016GL072259. [PubMed: 34646054]

Williams RME, Moersch JE, Fergason RL, 2018. . 10.1029/2018EA000402 13 pp.

Wilson SA, Morgan AM, Howard AD, Grant JA, 2021. The global distribution of craters with alluvial fans and deltas on Mars. Geophys. Res. Lett 10.1029/2020GL091653.

Zaki AS, Pain CF, Edgett KS, Gigengack R, 2018. Inverted stream channels in the Western Desert of Egypt: synergistic remote, field observations and laboratory analysis on Earth with applications to Mars. Icarus 309, 105–124. 10.1016/j.icarus.2018.03.001.

Zaki AS, Pain CF, Edgett KS, Castelltort S, 2021. Global inventory of fluvial ridges on Earth and lessons applicable to Mars. Earth-Sci. Rev 216 (103561). 10.1016/j.earscirev.2021.103561 46 pp.

van Zalinge ME, Sparks RSJ, Cooper FJ, Condon DJ, 2016. Early Miocene large-volume ignimbrites of the Oxaya Formation, Central Andes. J. Geol. Soc 173 (5), 716–733. 10.1144/jgs2015-123.

Zanbak C, Arthur RC, 1986. Environ. Eng. Geosci xxiii (4), 419–433. 10.2113/gseegeosci.xxiii.4.419.

NASA Author Manuscript

NASA Author Manuscript

NASA Author Manuscript

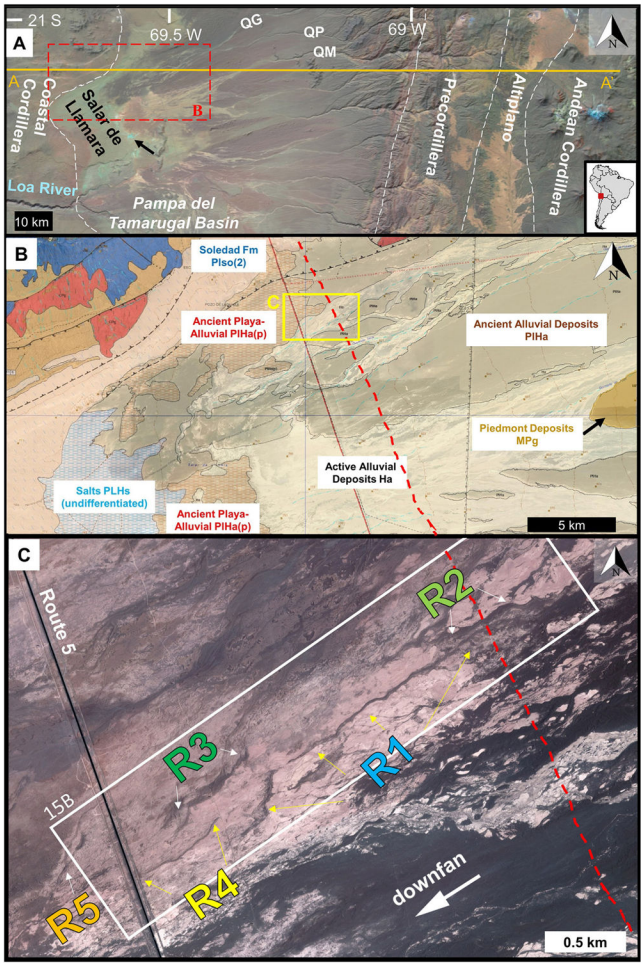

Fig. 1.

Several context images for the study site are presented. A) Regional view of the field site near Salar de Llamara is shown on false color Landsat image. Coalescing alluvial fans at the study site derive sediment primarily from two canyons, perennial flow through Quebrada Guatacondo (QG) and ephemeral flow in Quebrada de Pintados (QP) [minor contributions from Quebrada Mani (QM)] that terminate in the Pampa del Tamarugal basin (PdT). Physiographic regions (from Jayne et al., 2016) are demarcated by dashed lines. Black arrow marks groundwater-sourced perennial pool. Orange line is location of topographic profile shown in Supplementary Fig. S1. Dashed red box outlines the geologic map for area surrounding study site is presented in panel B. B) Geologic map (Quezada et al., 2012; red box in panel A) overlain on Google Earth image (12/11/2006, Image©2020 Maxar Technologies) with the location of panel C marked (yellow box). See descriptions of geologic units in Supplementary Fig. S2. C) Satellite image (Quickbird MM128226) of region around study site (white box, and location of Fig. 15B) with ridge labels marked for gravel ridges (R1, R2, R3) and sulfate-capped ridges (R4, R5). The active zones on the fan are pale brown or yellow in color (e.g., most of the study region within white box), which differ from older fan surfaces that are covered by dark, wind-blown granules (e.g., lower right corner). The boundary between late Pleistocene playa and alluvial deposits (units PlHa

and $PlHa_p$), an inferred shoreline at ~815 m asl, is marked by red dashed line (in B and C, see also Supplementary Text S1 for additional details.)

NASA Author Manuscript
NASA Author Manuscript
NASA Author Manuscript

NASA Author Manuscript

NASA Author Manuscript

NASA Author Manuscript

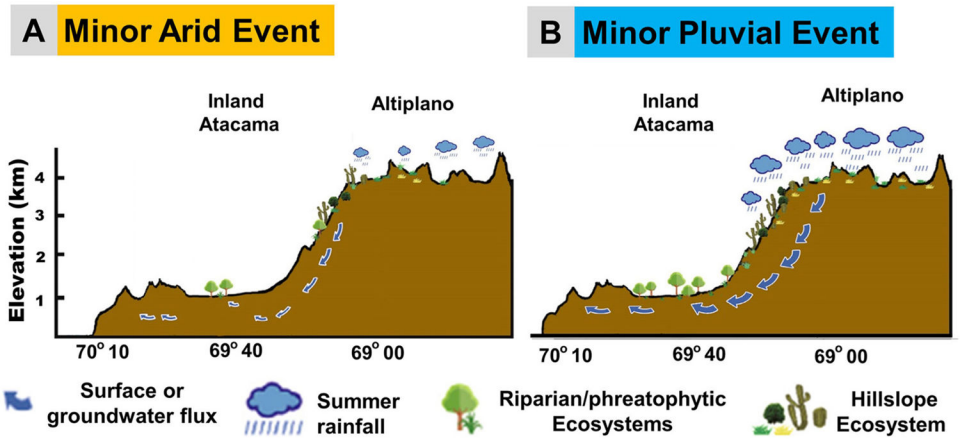

Fig. 2.

Schematic illustration contrasting minor climate variations associated with arid and pluvial events in the Chilean Atacama Desert caused by changes in rainfall at altitude. These periods were within an overall arid regime in the Central Depression, and the sketch exaggerates the differences in water and vegetation. See Section 2.2 for details. Figure after Santoro et al. (2017).

NASA Author Manuscript

NASA Author Manuscript

NASA Author Manuscript

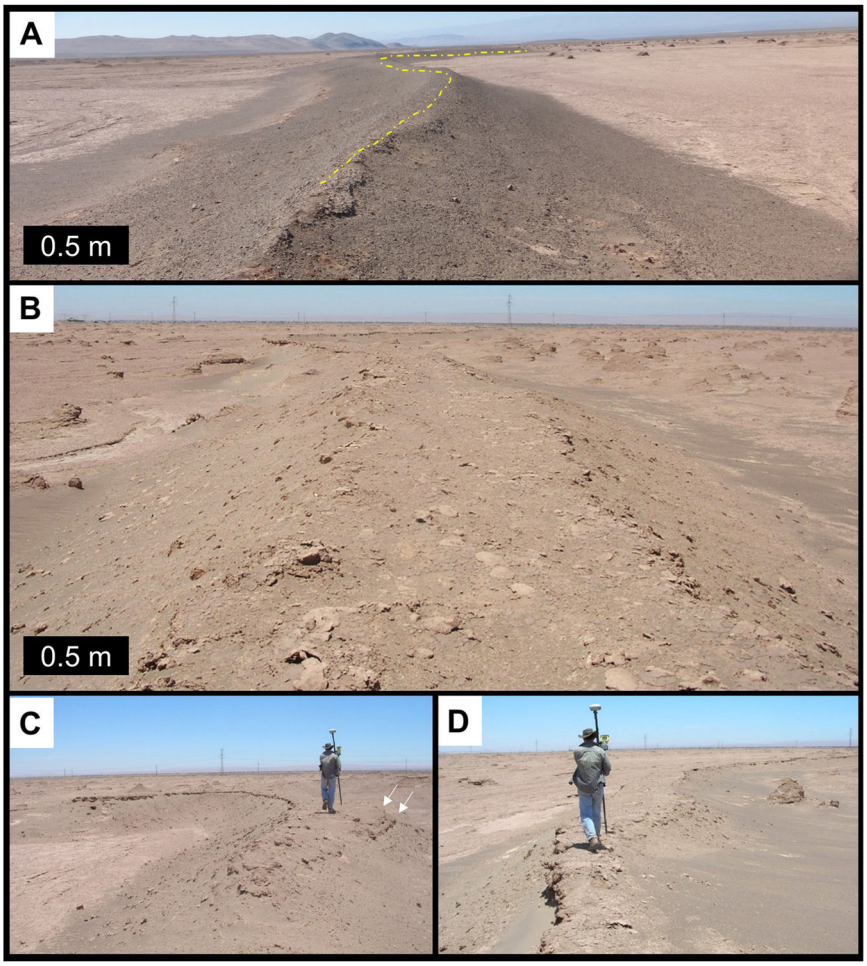

Fig. 3.

Top panels show along-ridge views of gravel-capped ridge R1 (A) and sulfate-capped ridge R4 (B). A) View to the northeast along gravel-capped ridge R1 illustrating the semi-curving path (dashed yellow line) and the narrow, rounded transverse ridge shape. B–D) Illustrations of ridge R4 with well-indurated sulfate cap in field photos viewed to the southwest. B) View along ridge R4 with bend to left in background, and yardangs on either side of ridge. Light-toned sulfate discs are prominent in foreground, where ridge width is ~3 m. C) Field photo of spur on ridge R4 located near 21.1194° S, 69.5788°W. White arrows mark two indurated levels in the upper unit of ridge R4. D) Section of ridge R4 with a narrow capstone. Side slopes are dark due to presence of gravels. Younger mudflows (light tan color) are present at left in panels C and D.

NASA Author Manuscript

NASA Author Manuscript

NASA Author Manuscript

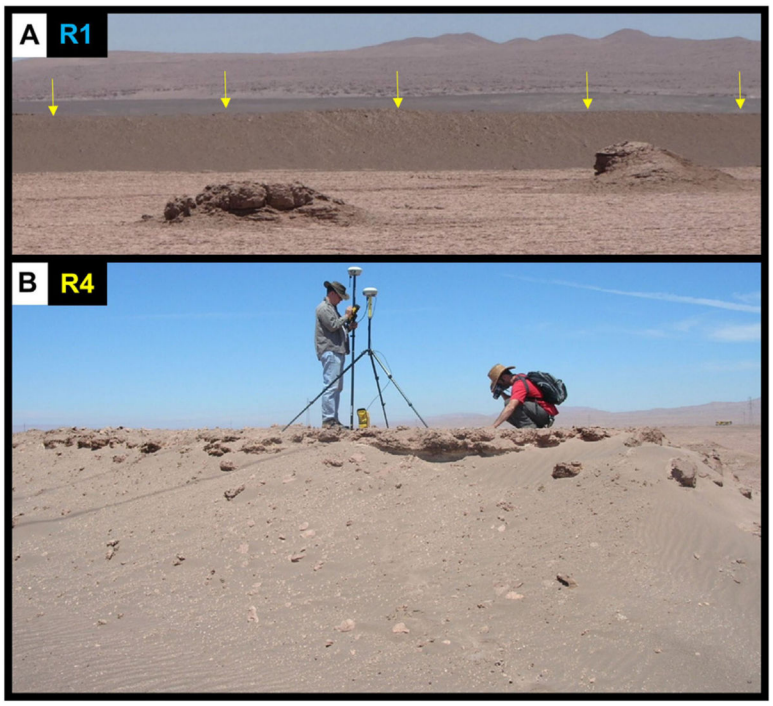

Fig. 4.

Side views of gravel-capped ridge R1 (A) and sulfate-capped ridge R4 (B). Both ridges have gravel clasts on the side slopes, with a greater density on ridge R1. A) Gravel-capped ridge is ~75 m wide in scene. Yellow arrows mark the ridge R1 crest, to aid in discriminating it from the dark background. Two yardangs in the foreground have similar orientation to the ridge, with a wider section facing downwind (southwest), and a tapered point to the northeast. B) The sulfate capstone is prominent along the length of ridge R4. Photo covers ~8 m long section of ridge.

NASA Author Manuscript NASA Author Manuscript NASA Author Manuscript

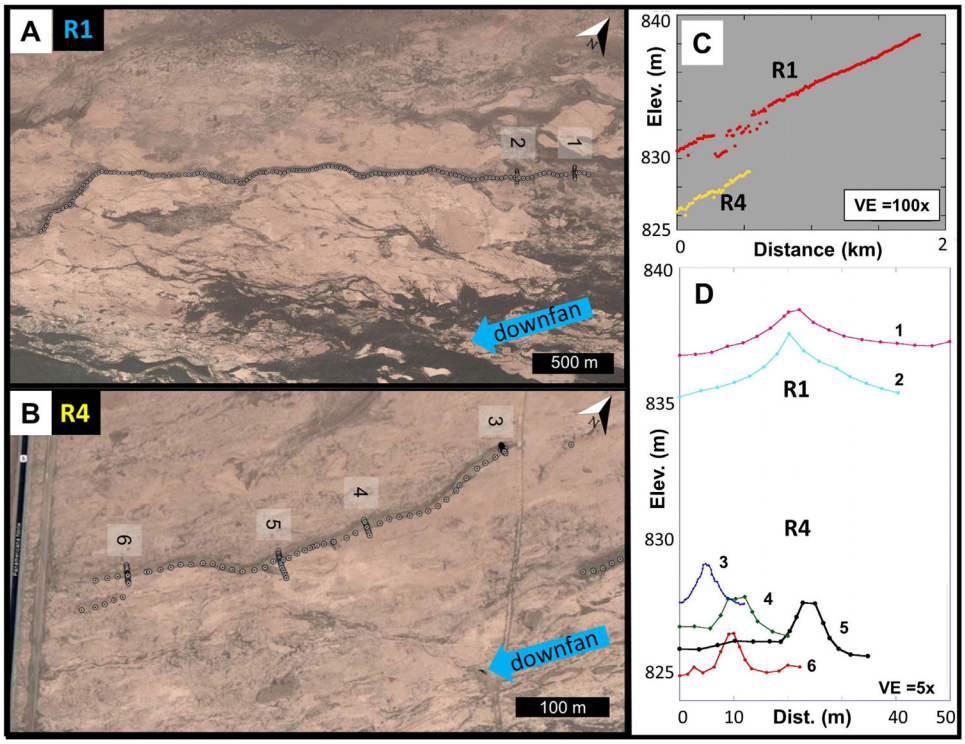

Fig. 5.

Longitudinal and cross-sectional GPS topographic survey locations marked on satellite image (Quickbird MM128226) of gravel-capped ridge R4 (A) and sulfate-capped ridge R1 (B). C) Longitudinal profiles for ridges R4 and R1 have origin (x = 0) set at downslope extent (i.e., topographic profile is from southwest to northeast). Along-ridge profiles correspond to a slope of 0.5%, and matches regional gradient. Locations of erosion (gaps along the ridge) were included in the topographic survey (maintaining consistent spacing of data collection), and these locations have lower elevation than the upper surface trendline. D) Six cross-sectional profiles are shown, with locations marked by number in panels A and B. For ridge R4 the profiles illustrate the rectangular form (profiles 4 and 5) and range in top width (1–3 m).

NASA Author Manuscript

NASA Author Manuscript

NASA Author Manuscript

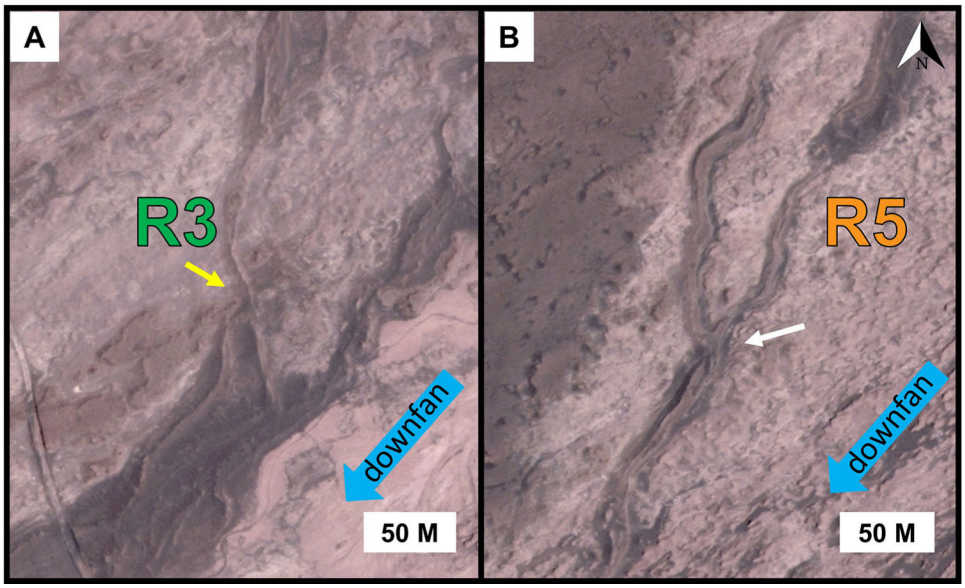

Fig. 6.

Illustration of different planimetric patterns associated with each ridge type. Regional gradient is downslope to lower left in both panels. A) Example of gravel-capped ridge R3 that bifurcates downslope. Ridge R3 is located near −21.114321°, −69.57602°. B) Example of sulfate-capped ridge R5 that joins an adjacent ridge downslope. Ridge R5 is located near −21.119815°, −69.585104°.

NASA Author Manuscript

NASA Author Manuscript

NASA Author Manuscript

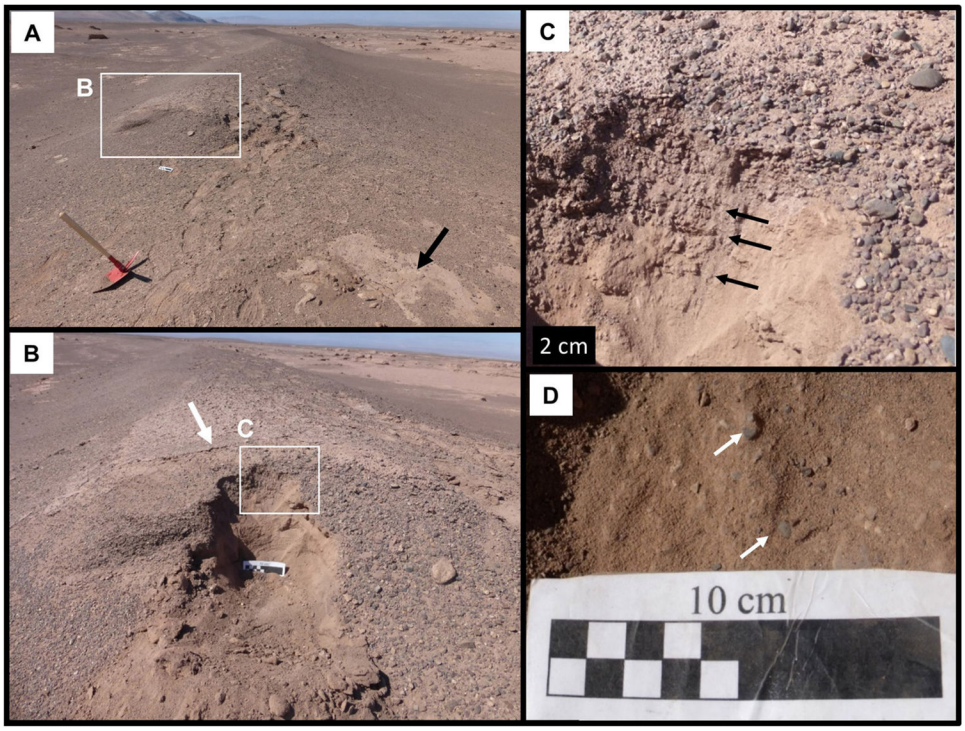

Fig. 7.

A) Example of gravel-capped ridge R1 in field photo prior to excavation of hand-dug trench. Walking on the surface generates sunken footprints that are evident in photo. Black arrow points to nodular halite on lower flank. B) Vertical trench was cut down 0.5 m through unconsolidated sediment. Gravels are typically 1–3 cm in size, but occasionally larger clasts are observed (Fig. 8). Rounded crest is approximately 1 m wide. Scale card is 10 cm. White arrow marks weakly indurated efflorescent surficial salt crust. C) Gravel pavement on ridge surface overlying fine-grained material with weak horizontal layering (black arrows). D) Isolated gravels (white arrows) embedded in gravel-capped ridge R1 silt to fine-sand size sediment.

NASA Author Manuscript

NASA Author Manuscript

NASA Author Manuscript

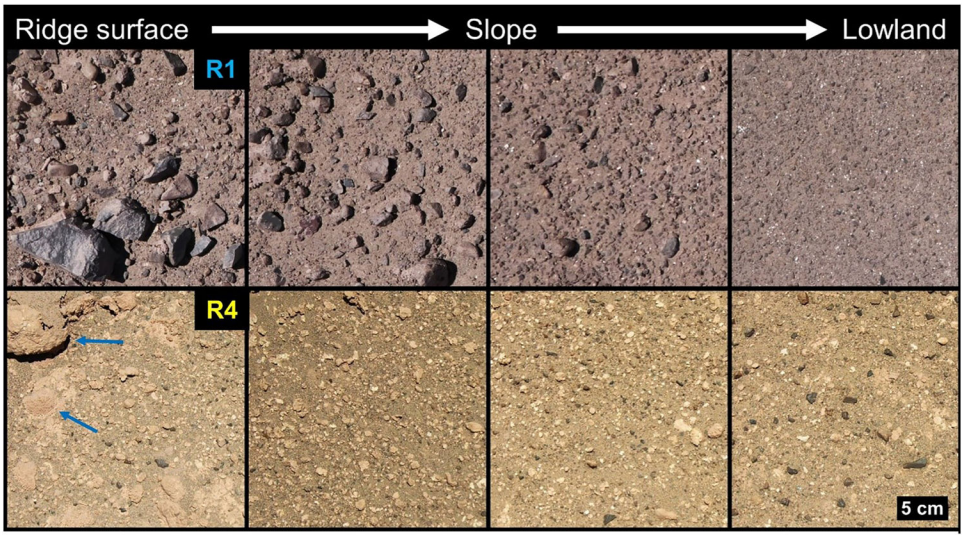

Fig. 8.

Illustrations of variation in grain size from ridge surface downslope (image sequence from left to right) for gravel-capped ridge R1 and sulfate-capped ridge R4 with each panel covering the same area. (Upper Row) Images from R1 show coarser clasts present at ridge crest and decreasing clast size as a function of distance downslope. Leftmost panel is rare example that includes small cobbles, whereas commonly the maximum clast size on the crest is 3 cm. The rightmost panel in the lowlands is exclusively fine gravel (granules) and sand. (Lower Row) For sulfate-capped ridges, the rounded black gravels are more common in the lowlands (rightmost panel) and are sparse on the ridge surface. Most of the surface area is covered by brown sand, and on the ridge surface there are also sulfate plates (some marked by blue arrows). See also Fig. 9.

NASA Author Manuscript

NASA Author Manuscript

NASA Author Manuscript

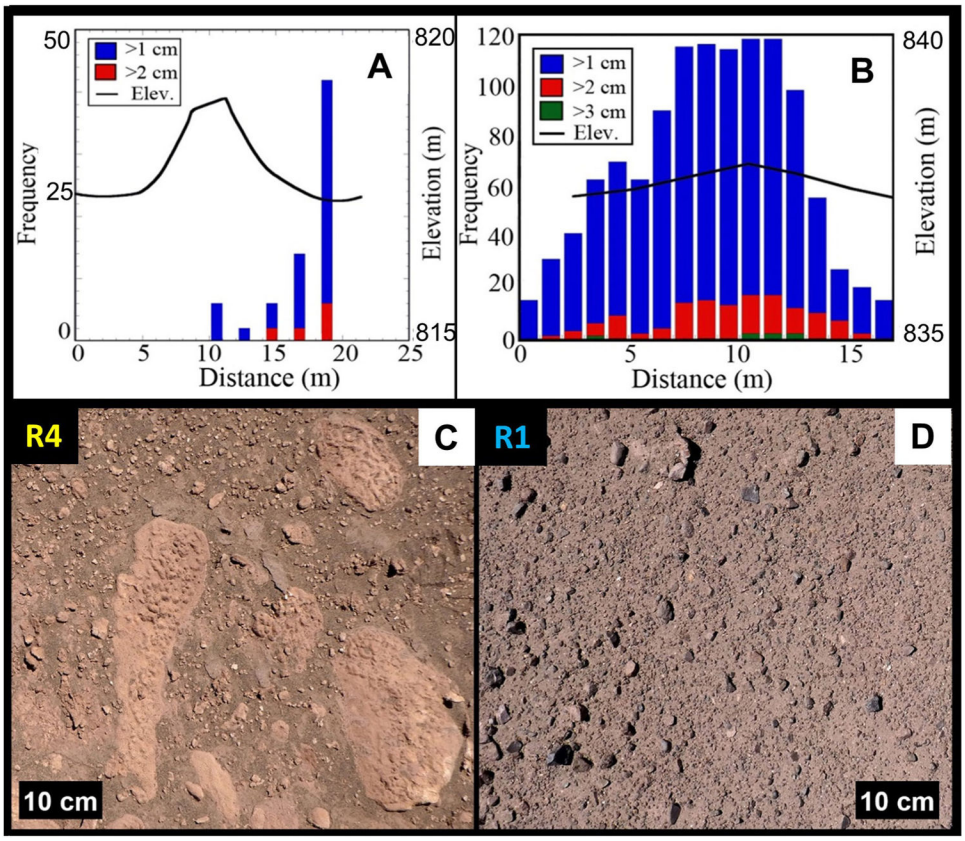

Fig. 9.

Differences in ridge cross-sectional shape and surface characteristics are illustrated for sulfate-capped ridge R4 (A and C) and gravel-capped ridge R1 (B and D). Panels A and B show binned grain size data for 1 m^2 area (100 counts, 10 cm grid spacing) at ridge crest, with frequency scale at left, and an overlain topographic profile (black line, vertical exaggeration 5×) with elevation axis at right. Photos of the ridge surface are illustrated in panels (C) and (D) with sulfate plates and few gravels present on ridge R4 and a gravel-covered surface on ridge R1.

NASA Author Manuscript

NASA Author Manuscript

NASA Author Manuscript

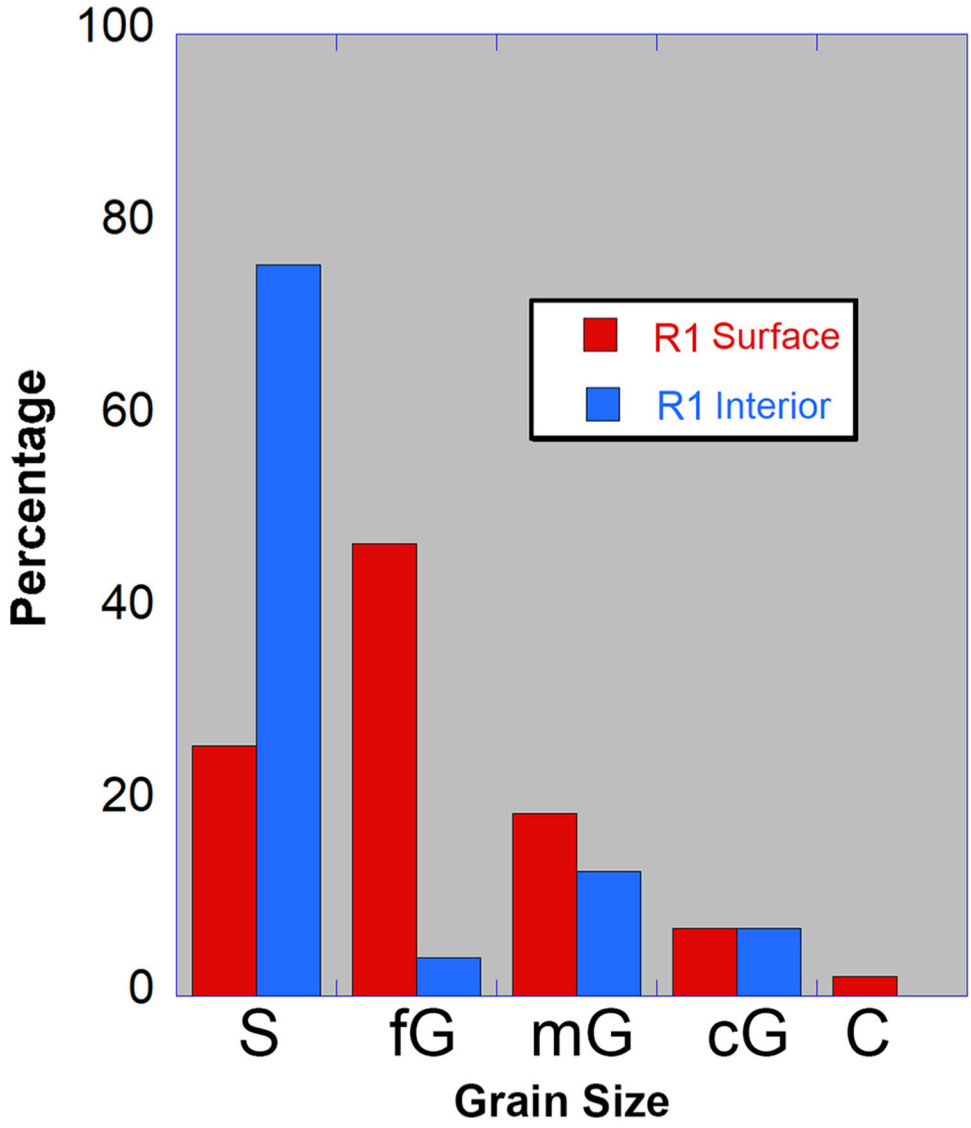

Fig. 10.

Histogram of grain size distribution at gravel-capped ridge R1 based on counts over a 0.2 m^2 area with 5 cm grid spacing ($n = 100$). The percentage of clasts were grouped into sand (S, or finer), fine, medium or coarse gravel (fG, mG, cG), and cobble (C). The size fraction below medium sand was not subdivided. Clasts on the ridge surface (red bars) have a unimodal distribution that is dominantly fine gravel, whereas the interior deposits (blue bars) are bimodal with sand as the dominant grain size and a minor peak at medium gravel. The difference in grain size distribution is attributed to winnowing of fines resulting in a coarser surface deposit.

NASA Author Manuscript

NASA Author Manuscript

NASA Author Manuscript

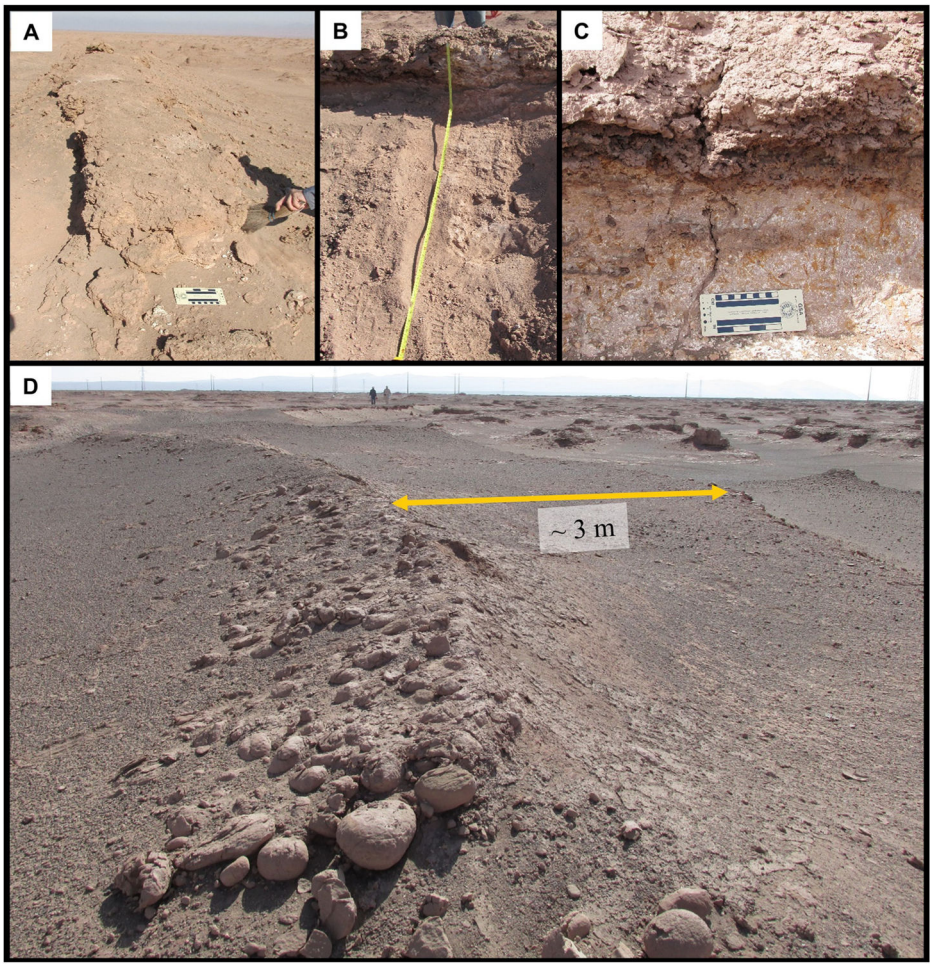

Fig. 11.

Field photos to illustrate ridge R5, a sulfate-capped ridge. A) Rectangular transverse shape of sulfate capstone at ridge R5. Black scale bar is 10 cm. B) Photo of the ridge R5 flank. Total relief shown is 1.2 m. C) Close-up of ridge R5 capstone which has textural similarity to the R4 ridge capstone. Iron-stained root traces are evident in the light-toned layer. Black scale bar is 10 cm. D) The crest of ridge R5 is concave and ~3 m wide. Rarely, there are areas with ignimbrite cobbles (up to 10 cm diameter), interpreted as a marginal deposit along the former R5 channel. People are walking on ridge in background.

NASA Author Manuscript

NASA Author Manuscript

NASA Author Manuscript

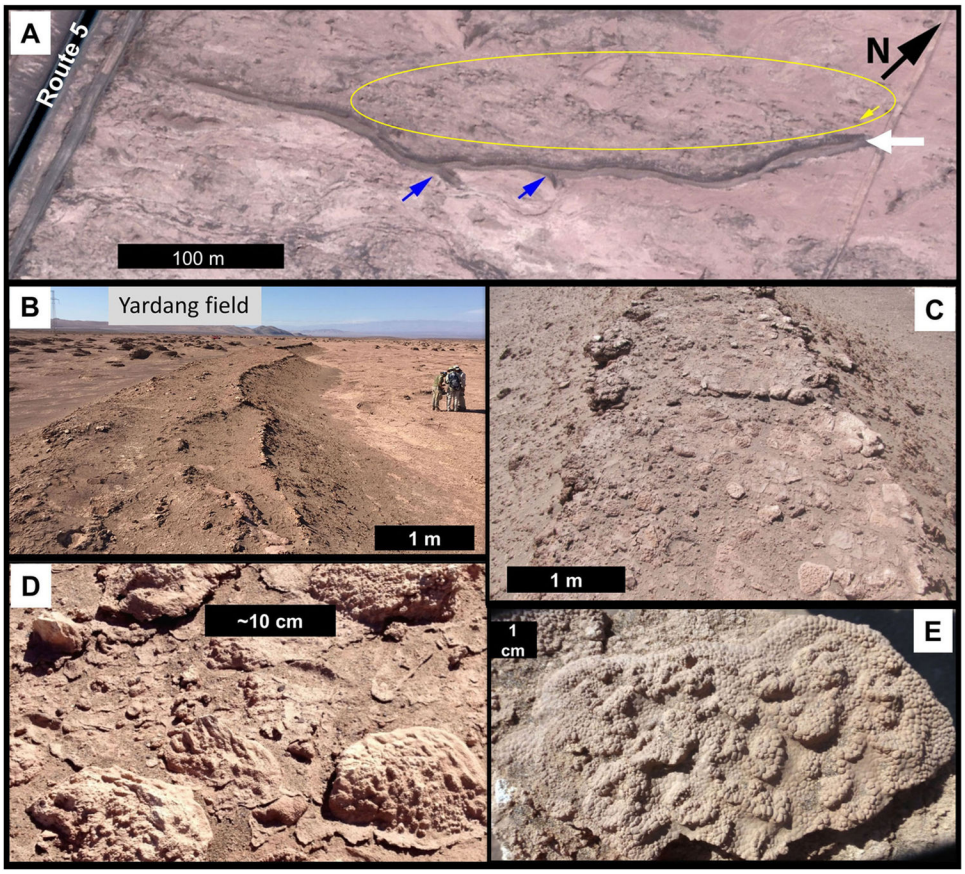

Fig. 12.

Examples of sulfate domes and plates associated with sulfate-capped ridge R4. A) Ridge R4 is a relatively linear ridge aligned roughly N30E and has two short spur segments (blue arrows; see also Fig. 3C) in Quickbird image MM128226. A vertical trench was cut at the northeastern edge of ridge R4 (white arrow). Yellow oval outlines a portion of the yardang field (northeast alignment), and the yellow arrow marks location of a nearby yardang where a vertical trench was made (Supplementary Fig. S3). Downfan direction is to the left. B) Perspective upslope view of ridge R4, with rectangular cross-sectional form and concave surface (raised margins) capped by sulfate discs. C) Enlargement of ridge R4 top surface to show the discrete sulfate discs capping the ridge. D) Oblique photograph of gypsum domes and plates on ridge surface. E) Close-up photograph of gypsum plate with bumpy ‘goosebump’-like texture.

NASA Author Manuscript

NASA Author Manuscript

NASA Author Manuscript

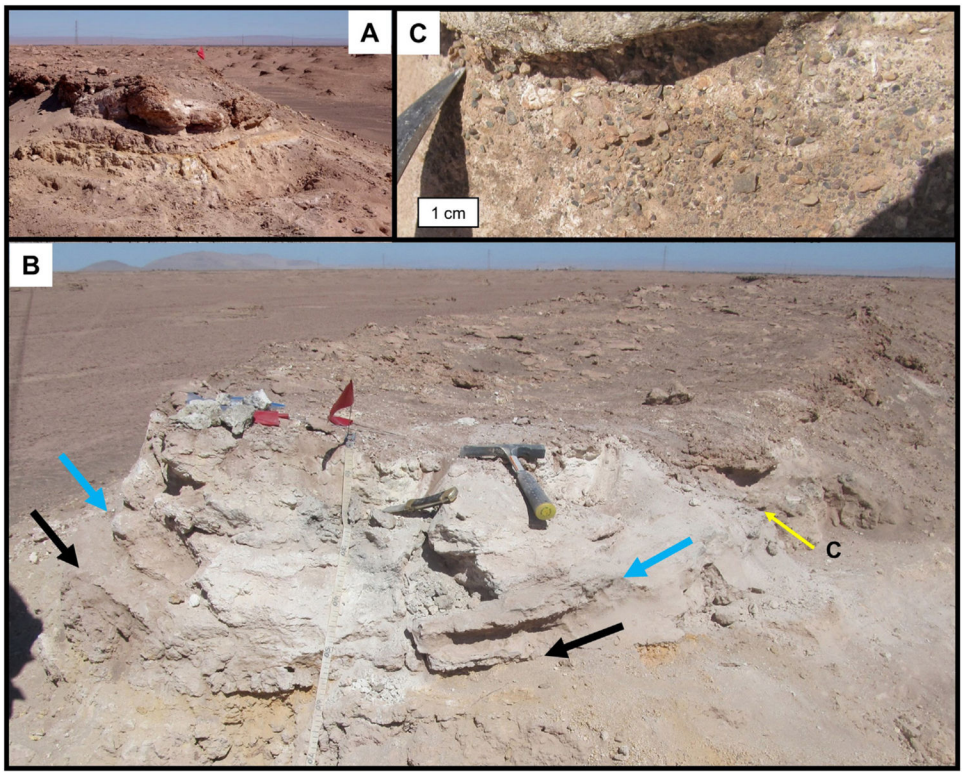

Fig. 13.

Some layers in sulfate-capped ridge R4 have concave form. A) Photo taken of brushed ridge R4 outcrop prior to excavation with shovels. Ridge width at top is 1.5 m. B) Post-excavation photo of R4 outcrop. Concave shape is particularly evident in two resistant layer components, with blue arrow marking base of upper unit, and black arrow marking a layer in the lower unit. The distinctive orange layer also has a concave form but is partially covered in this photo; see Figs. 14B and 16C. Yellow arrow points to enlargement in panel C. C) Close-up of gravel lens in a fine-grained sandstone layer at the boundary between the lower and upper units. Polymict fine to medium gravels are subrounded to rounded in shape and interpreted as a pocket of streamflow deposits.

NASA Author Manuscript

NASA Author Manuscript

NASA Author Manuscript

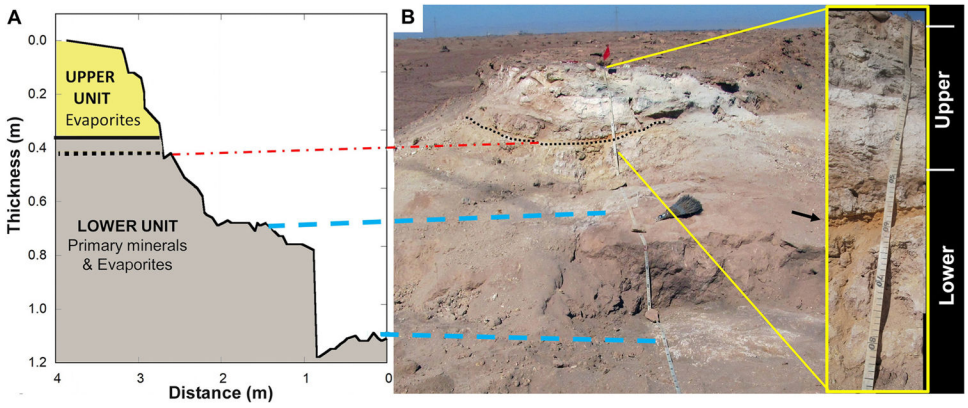

Fig. 14.

Simplified stratigraphic section at sulfate capped R4 ridge. A) Transverse relief profile of northeastern edge of ridge R4 (white arrow in Fig. 12A). Ridge R4 is compositionally subdivided into an upper unit comprised of evaporite minerals, and a lower unit with evaporites and primary minerals (Noe Dobrea et al., 2017). Two stair-steps in the profile correspond to anhydrite-rich hardpans (dashed blue lines) that correlate regionally (Supplementary Fig. S3). B) Photograph of trenched section of ridge R4. The topographic survey shown in panel A was conducted along tape measure. Dotted black line corresponds to trace of thin, orange layer (dash-doted red line identifies location in topographic panel in panel A, and black arrow in enlargement). Close-up view of top section (~0.6 m) is presented at far right to illustrate color and textural variations. Shadow from power line diagonally crosses lower portion of outcrop. See Supplementary Table S2 for color descriptions of layers in ridge R4.

NASA Author Manuscript

NASA Author Manuscript

NASA Author Manuscript

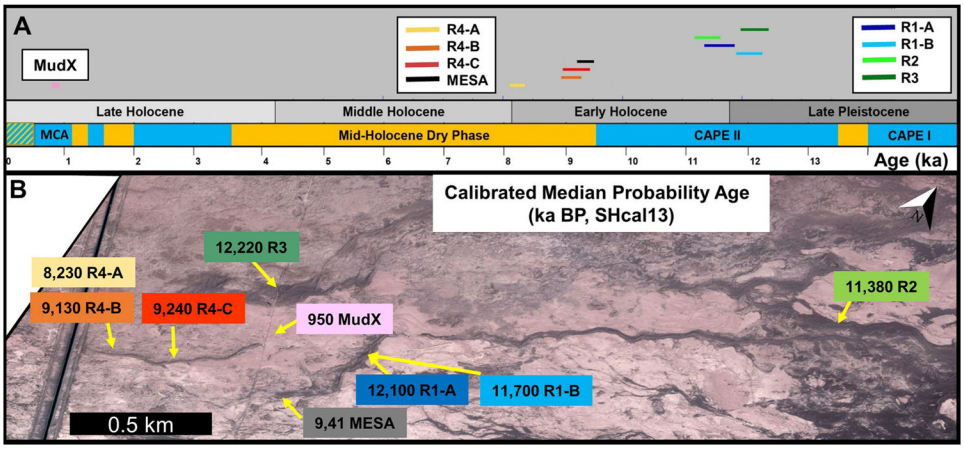

Fig. 15.

Summary of radiometric dates for nine wood samples from field site and association with minor paleoclimatic variations. A) Calibrated 2σ age range reported per sample relative to geologic epoch and reconstructed climate periods for the Pampa del Tamarugal basin. Periods are color coded to represent minor climatic fluctuations within overall arid conditions, with relatively wet pulses (blue bars), somewhat drier conditions (orange bars) periods, and intermixed wet and arid (patterned blue/orange) during the last 0.5 ka, as reported in Santoro et al. (2017). MCA: Medieval Climate Anomaly. CAPE: Central Andean Pluvial Event. B) Location of sample sites (color legend in panel A insets) are labeled with calibrated median probability age on Quickbird image MM128226. At this scale, some samples are co-located (R1-A & R1-B; R4-A & R4-B). Additional sample details are in Table 1. See Fig. 1B for location of this satellite subscene.

NASA Author Manuscript

NASA Author Manuscript

NASA Author Manuscript

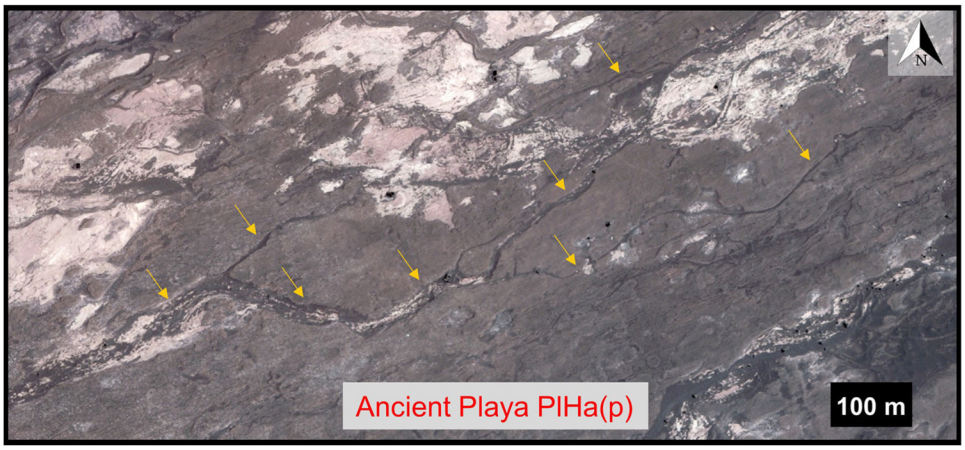

Fig. 16.

Example of contributory channel network (orange arrows) incised into ancient playa deposits at a location downslope from study site (Quickbird image MM128226). Light tan areas are mudflow deposits infilling topographic lows.

NASA Author Manuscript

NASA Author Manuscript

NASA Author Manuscript

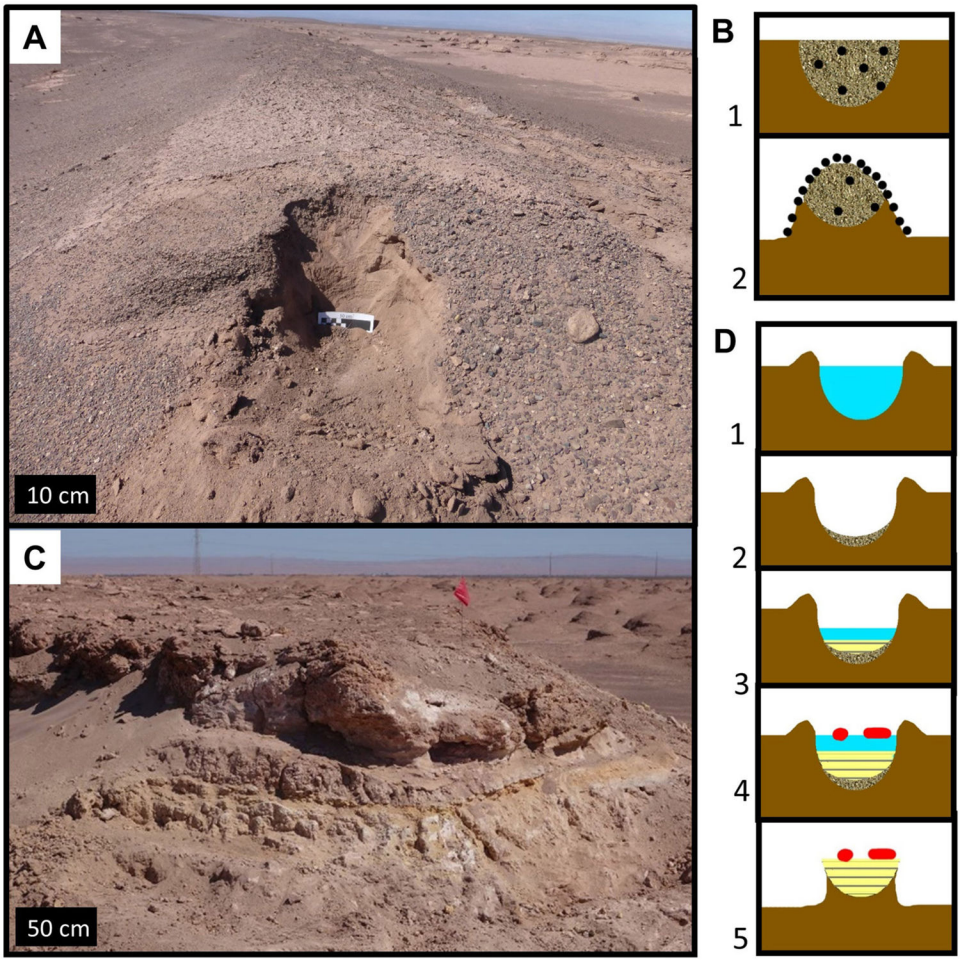

Fig. 17.

Comparison of proposed evolutionary sequence for two ridge types at Salar de Llamara, Chile. In both models, the brown layer represents the surrounding materials, presumed to be ancient alluvial/playa deposits. Gravel–capped ridges (A) are interpreted as mudflow deposits with a bimodal grain size distribution (B1) that were deflated by aeolian erosion that removed the finer component and left a residual gravel lag (B2). Sulfate-capped ridges (C) are former sites of a channel (D1) that may have had overbank levees. In panel D, brown corresponds to lower unit, sand texture for channel deposits, yellow for evaporites in upper unit, and red for sulfate plates. Over time, the abandoned channel (D2) was episodically filled with an evaporative sequence (yellow, D3) that formed via groundwater precipitation (possibly ponded) or backed-up surface flow into a lake. At a later time, changes in the chemistry of ponded water facilitated gypsum domes and/or microbial mats (red dots in D4), and their residual are sulfate plates on the surface of the deflated ridge today (D5). Wind erosion stripped the overbank deposits, if any, as well as country rock, resulting in the inverted channel. Surface-conforming halite is found on the flanks of both ridge types and is interpreted to form after topographic inversion took place as a consequence of remobilization of soluble salts.

NASA Author Manuscript

NASA Author Manuscript

NASA Author Manuscript

Table 1

Grain size characteristics of Atacama fan sediments.

Description	Percentage			Facies
	Sand	Gravels	Cobbles	
R1 Surface	25	60	15	Coarse sandy gravel (csG)
R1 interior	75	25	0	Gravelly sand (gS)
Upstream mudflow deposits[a]	79	21	0	Gravelly sand (gS)
Channel bank deposits[a]	90	10	0	Sand (S)
Overbank sediment[a]	100	0	0	Sand (S)

[a]Data from Morgan et al. (2014).

NASA Author Manuscript
NASA Author Manuscript
NASA Author Manuscript

Table 2

Sample Locations, AMS ^{14}C and calibrated dates for wood samples collected in this study.

Sample name	Laboratory code	Location		^{14}C	^{14}C	^{14}C
		Lat	Long		2σ	Probability age
		(°S)	(°W)	(cal kyr BP)	(cal kyr BP)	(cal kyr BP)
MudX	OS-127718	21.116950	69.576450	1100 ±20	930–980	950
R4-A	OS-141583	21.119950	69.580043	7430 ± 35	8160–8340	8230
R4-B	OS-141584	21.109170	69.585381	8220 ± 50	9010–9280	9130
R4-C	OS-127721	21.119039	69.578444	8300 ± 75	9030–9430	9240
MESA	OS-141587	21.117982	69.575116	8420 ± 45	9270–9500	9410
R1-A	OS-141585	21.115605	69.573801	10,350 ± 50	11,930–12,320	12,100
R1-B	OS-141586	21.115498	69.573786	10,150 ± 50	11,400–11,850	11,700
R2	OS-141582	21.106569	69.562681	10,000 ± 45	11,240–11,610	11,380
R3	OS-141716	21.115439	69.577206	10,400 ± 50	12,000–12,420	12,220

Geomorphology (Amst). Author manuscript; available in PMC 2021 November 15.